Cell Stem Cell

Article

Osteopontin drives neuroinflammation and cell loss in *MAPT-N279K* frontotemporal dementia patient neurons

Graphical abstract

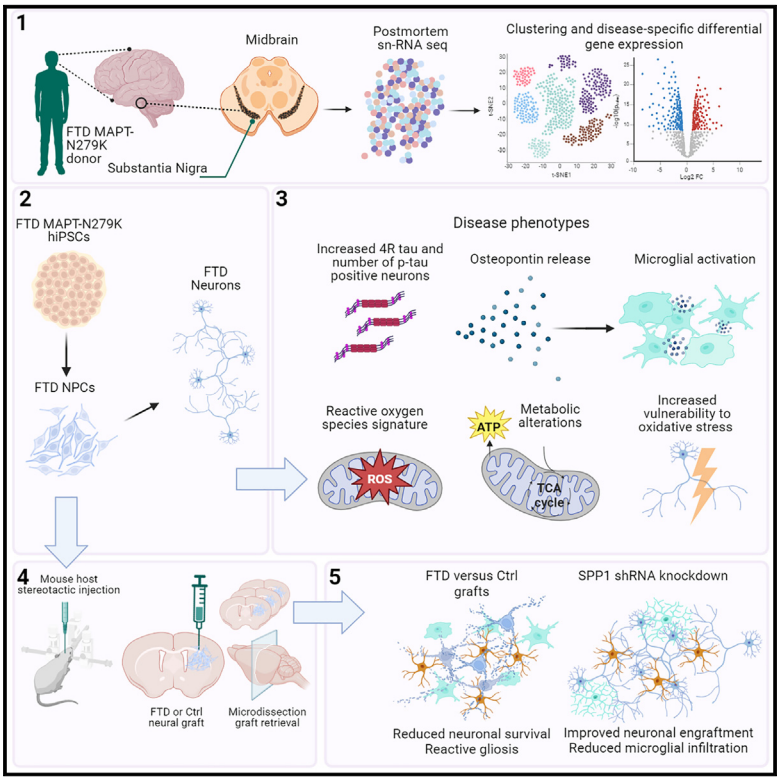

Highlights

- Postmortem and iPSC-derived FTD neurons upregulate inflammatory genes, including SPP1
- FTD neurons show mitochondrial phenotypes partially rescued by SPP1 knockdown
- Grafted FTD neurons show impaired cell survival and elevate reactive gliosis
- Knockdown of SPP1 in FTD neurons improves engraftment and reactive gliosis

Authors

Osama Al-Dalahmah, Matti Lam, Julie J. McInvale, ..., Vilas Menon, Peter Canoll, Gunnar Hargus

Correspondence

gh2374@cumc.columbia.edu

In brief

Hargus and colleagues demonstrate that iPSC-derived FTD neurons and human postmortem FTD neurons show phenotypes related to mitochondrial function and neuroinflammation, including an upregulation of osteopontin. Transplanted FTD neurons show impaired survival and elicit an increased microglial response, which is partially rescued by downregulation of osteopontin in transplanted cells.

Al-Dalahmah et al., 2024, Cell Stem Cell *31*, 1–18
May 2, 2024
https://doi.org/10.1016/j.stem.2024.03.013

CellPress

Cell Stem Cell

CellPress
OPEN ACCESS

Article

Osteopontin drives neuroinflammation and cell loss in *MAPT-N279K* frontotemporal dementia patient neurons

Osama Al-Dalahmah,[1,2,11] Matti Lam,[3,11] Julie J. McInvale,[1,11] Wenhui Qu,[1] Trang Nguyen,[1] Jeong-Yeon Mun,[1] Sam Kwon,[1] Nkechime Ifediora,[1] Aayushi Mahajan,[4] Nelson Humala,[4] Tristan Winters,[1] Ellen Angeles,[2] Kelly A. Jakubiak,[1] Rebekka Kühn,[1] Yoon A. Kim,[1] Maria Caterina De Rosa,[5] Claudia A. Doege,[1] Fahad Paryani,[3] Xena Flowers,[1] Athanassios Dovas,[1] Angeliki Mela,[1] Hong Lu,[1] Michael A. DeTure,[6] Jean Paul Vonsattel,[1] Zbigniew K. Wszolek,[7] Dennis W. Dickson,[6] Tanja Kuhlmann,[8] Holm Zaehres,[9,10] Hans R. Schöler,[10] Andrew A. Sproul,[1,2] Markus D. Siegelin,[1] Philip L. De Jager,[2,3] James E. Goldman,[1,2] Vilas Menon,[2,3] Peter Canoll,[1] and Gunnar Hargus[1,2,12,*]

[1]Department of Pathology & Cell Biology, Columbia University, New York, NY 10032, USA
[2]Taub Institute for Research on Alzheimer's Disease & the Aging Brain, Columbia University, New York, NY 10032, USA
[3]Center for Translational & Computational Neuroimmunology, Department of Neurology, Columbia University Irving Medical Center, New York, NY 10032, USA
[4]Department of Neurosurgery, Columbia University, New York, NY 10032, USA
[5]Division of Molecular Genetics, Department of Pediatrics, Columbia University, New York, NY 10032, USA
[6]Department of Neuroscience, The Mayo Clinic Florida, Jacksonville, FL 32224, USA
[7]Department of Neurology, The Mayo Clinic Florida, Jacksonville, FL 32224, USA
[8]Institute of Neuropathology, University Hospital Münster, Münster 48149, Germany
[9]Institute of Anatomy, Ruhr University Bochum, Medical Faculty, Bochum 44801, Germany
[10]Max Planck Institute for Molecular Biomedicine, Münster 48149, Germany
[11]These authors contributed equally
[12]Lead contact
*Correspondence: gh2374@cumc.columbia.edu
https://doi.org/10.1016/j.stem.2024.03.013

SUMMARY

Frontotemporal dementia (FTD) is an incurable group of early-onset dementias that can be caused by the deposition of hyperphosphorylated tau in patient brains. However, the mechanisms leading to neurodegeneration remain largely unknown. Here, we combined single-cell analyses of FTD patient brains with a stem cell culture and transplantation model of FTD. We identified disease phenotypes in FTD neurons carrying the *MAPT-N279K* mutation, which were related to oxidative stress, oxidative phosphorylation, and neuroinflammation with an upregulation of the inflammation-associated protein osteopontin (OPN). Human FTD neurons survived less and elicited an increased microglial response after transplantation into the mouse forebrain, which we further characterized by single nucleus RNA sequencing of microdissected grafts. Notably, downregulation of OPN in engrafted FTD neurons resulted in improved engraftment and reduced microglial infiltration, indicating an immune-modulatory role of OPN in patient neurons, which may represent a potential therapeutic target in FTD.

INTRODUCTION

Frontotemporal dementia (FTD) is a group of neurodegenerative diseases and a major cause of dementia in patients under 60 years of age without treatment options. About half of patients have widespread deposition of hyperphosphorylated tau (p-tau) protein in various brain regions, including the frontal and temporal lobes, as well as basal ganglia and brain stem (FTD-tau). A family history is seen in about half of the patients with FTD, and 10%–30% of these patients carry autosomal-dominant mutations in *MAPT* on chromosome 17q21 encoding tau.[1]

Tau is expressed as six different isoforms in the adult human brain as the result of alternative splicing of exons 2, 3, and 10 with equal amounts of 3R tau and 4R tau isoforms in the healthy brain containing either 3 or 4 microtubule-binding domains, respectively.[2,3] In many FTD patients with tau pathology, this 3R:4R tau ratio is shifted toward 4R isoforms, forming the group of 4R-tauopathies with abundant deposition of p-tau in neurons, astrocytes, and oligodendrocytes.[4,5] The presence of p-tau is linked to cellular dysfunction since it leads to detachment of tau from microtubules with intracellular accumulation of p-tau, collapse of intracellular transport, and synaptic breakdown.[6,7] Tau interacts with several mitochondrial proteins associated with the mitochondrial respiratory chain,[8,9] raising the possibility that alterations in tau might also induce mitochondrial dysfunction.

Please cite this article in press as: Al-Dalahmah et al., Osteopontin drives neuroinflammation and cell loss in *MAPT-N279K* frontotemporal dementia patient neurons, Cell Stem Cell (2024), https://doi.org/10.1016/j.stem.2024.03.013

There is evidence that neuroinflammation plays an important role in the pathogenesis of FTD. Microglial activation is found in areas of neuronal loss[10] and increased p-tau burden[11] and in close proximity to p-tau-containing cells in patients and animal models of FTD.[12] PET imaging[13] and biomarker studies[14] also documented increased neuroinflammation in FTD patient brains and cerebrospinal fluid (CSF), respectively.

Here, we performed single-cell analyses on postmortem brain tissue from FTD patients carrying the *MAPT-N279K* mutation and from control (Ctrl) individuals combined with functional validation studies using a human *MAPT-N279K*-induced pluripotent stem cell (iPSC) model of FTD *in vitro* and after transplantation into the adult mouse brain. The *MAPT-N279K* mutation is located in exon 10 and is one of the most common *MAPT* mutations, leading to mis-splicing of tau toward 4R tau isoforms and causing severe neuronal and glial p-tau pathology in forebrain and hindbrain areas.[4,15] Patients expressing tau-N279K develop early symptoms at an age of 43.8 ± 6.7 years with involvement of the substantia nigra (SN), leading to a Parkinson's disease (PD)-like movement disorder.[15–17] Our findings indicate that FTD-tau patient neurons have an intrinsically altered mitochondrial function and carry an immune-modulatory role, resulting in an altered microglial response when transplanted into the mouse brain.

RESULTS

Neuronal loss and microgliosis in the SN of FTD-tau patients

We performed histological analyses of brain tissue of *MAPT-N279K* FTD patients and of Ctrl individuals (Figure 1; demographics given in Table S1). Since the SN is involved early in *MAPT-N279K* FTD (henceforth termed FTD) and since the SN is a common site of degeneration in other hereditary and non-hereditary forms of FTD,[15–17] it was chosen to study differential cell vulnerability and neuroinflammation. We quantified the areas of the SN pars compacta (SN-PC) and SN pars reticulata (SN-PR) in the two groups and found a significant reduction in the size of both areas in the FTD group (Figures 1A–1C). We also quantified neuronal numbers in the SN (Figure 1D) and found large, significant reductions in SN-PC and SN-PR neurons in the FTD group (Figures 1E and 1F), associated with abundant neuropil threads and neurofibrillary tangles composed of p-tau (Figure 1G). Neuronal dropout was paralleled by a significant increase in glial profiles (Figures 1H and 1I) in the same regions. Activated $CD68^+$ microglia were significantly increased in both the FTD SN-PC and SN-PR (Figures 1J–1L), indicating that the increase in glial nuclei is accounted for, at least in part, by an increase in reactive microglia.

We next microdissected the SN from frozen postmortem brain tissue from four Ctrl individuals and eight FTD donors carrying *MAPT-N279K* and performed transcriptional profiling using RNA microarrays (Figures 1M and 1N). Examination of the top differentially expressed genes (DEGs) revealed that microglial genes like complement *C3*, pro-phagocytic *TYROBP*, and *MSR1* were increased in the FTD group. Conversely, neuronal genes like the dopamine transporter *SLC6A3*, tyrosine hydroxylase (*TH*), and the GABA (gamma-aminobutyric acid) receptor gene *GABRA4* were decreased in FTD (Figure 1M; Table S2). Active sub-pathway enrichment analysis reveals that the spliceosome KEGG (Kyoto Encyclopedia of Genes and Genomes) pathway was highly enriched in the DEGs in the FTD group, which could, at least in part, be related to known mis-splicing of tau toward increased 4R isoforms in *MAPT-N279K* carriers,[18] as also identified in our patients (Figures S1A and S1B). Moreover, several immune-activation-related KEGG pathways were enriched, including JAK-STAT (Janus kinase-signal transducer and activator of transcription) signaling, NOD (nucleotide-binding oligomerization domain)-like receptor signaling, and infection-related pathways (Figure 1N).

snRNA-seq implicates oxidative phosphorylation and inflammation in neuronal dysfunction in FTD

To assign transcriptional pathology to single-cell types, we performed single nucleus RNA sequencing (snRNA-seq) on microdissected frozen postmortem SN tissue from six FTD and seven Ctrl donors (Figures 2A and S1C). Our analysis identified 10,752 nuclei (4,882 Ctrl and 5,870 FTD nuclei) (Figure 2B). Unbiased clustering and major cell-type classification identified neurons, astrocytes, oligodendrocytes, oligodendrocyte precursors, and microglia, and nuclei of the same lineage occupy largely non-overlapping uniform manifold approximation and projection (UMAP) space (Figures 2C and 2D). The expression of select cell-type markers is shown in Figure 2D.

To identify the genes that are changed in FTD-tau neurons, we performed differential gene expression analysis between FTD and Ctrl neuronal nuclei and identified 1,417 DEGs (Figure 2E; Table S2). Of these DEGs, the majority were downregulated (1,045 genes). Several were related to dopaminergic neuronal function, such as *TH* and the dopamine transporter *SLC6A3* (Table S2), consistent with depletion of nigral neurons in FTD-tau. Among the top DEGs increased in neurons was *APOE*, which is also increased in dopaminergic neurons in PD.[19] Moreover, several DEGs associated with immune functions, including *CD74*, *B2M*, and *C1QB*, were increased in FTD neurons (Table S2). KEGG pathway enrichment analysis of the DEGs (Figure 2F; Table S2) showed enrichment of neurodegenerative pathways (e.g., PD), proteasome, mitophagy, synaptic vesicle cycle, and mTOR (mammalian target of rapamycin) signaling. Interestingly, this analysis also revealed pathways involved in inflammation (e.g., EBV [Epstein-Barr virus] infection and interleukin [IL]-17 signaling) and oxidative phosphorylation. It is notable that ribosomal genes were also enriched, but the significance of this finding is not known.

The neuronal populations in the SN are heterogeneous. We subclustered them into four groups (Figures 2G–2I and S1D): dopaminergic (Neuron_DA), inhibitory (Neuron_Inh), RBFOX1 positive (Neuron_RBFOX1), and Calbindin-2 positive (Neuron_CALB2). Examination of select marker genes demonstrates the expression of *TH*, *SLC6A3*, and the monoamine transporter *SLC18A2* in Neuron_DA; the RNA-binding protein *RBFOX1*, *FGF12*, *ROBO2*, and the voltage-gated potassium channel interacting protein *KCNIP4* in Neuron_RBFOX1; *CALB2* and the glutamate transporters VGLUT1 and VGLUT2 (*SLC17A6* and *SLC17A7*) in Neuron_CALB2; and the glutamic acid decarboxylases *GAD1* and *GAD2*, GABA transporter

Please cite this article in press as: Al-Dalahmah et al., Osteopontin drives neuroinflammation and cell loss in *MAPT-N279K* frontotemporal dementia patient neurons, Cell Stem Cell (2024), https://doi.org/10.1016/j.stem.2024.03.013

CellPress
OPEN ACCESS

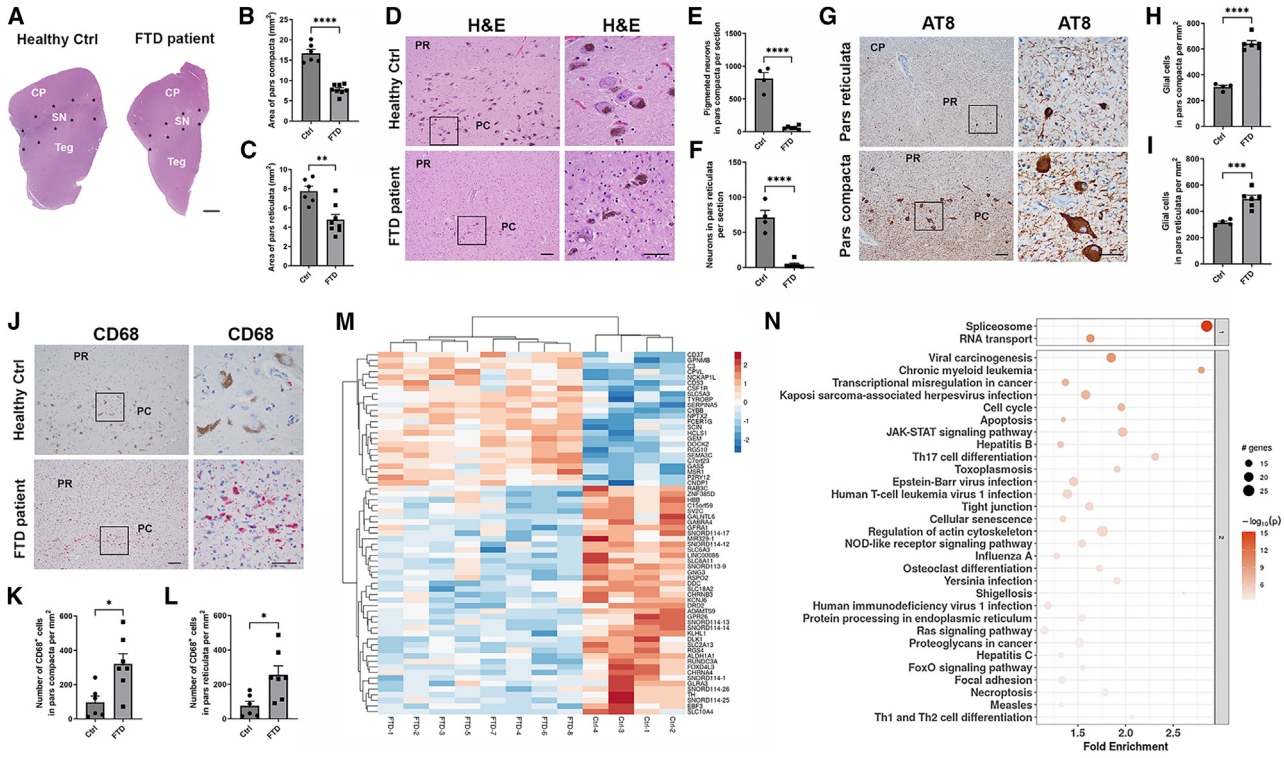

Figure 1. Histology and bulk RNA expression analysis of postmortem FTD and Ctrl substantia nigra

(A) Hematoxylin and eosin (H&E)-stained sections of the substantia nigra of a Ctrl and of an FTD patient. CP, cerebral peduncle; SN, substantia nigra; Teg, tegmentum.

(B) Quantification of the area of the pars compacta (PC).

(C) Quantification of the area of the pars reticulata (PR).

(D) H&E-stained sections of Ctrl and FTD SN with higher magnification.

(E) Quantification of neurons in the PC.

(F) Quantification of neurons in the PR.

(G) AT8 (p-tau)-stained sections of the FTD SN with higher magnification.

(H) Quantification of glial cells in the PC.

(I) Quantification of glial cells in the PR.

(J) CD68-stained sections of Ctrl and FTD SN with higher magnification.

(K) Quantification of $CD68^+$ cells in the PC.

(L) Quantification of $CD68^+$ cells in the PR.

(M) Heatmap of the top DEGs in the SN of FTD patients compared with Ctrl individuals.

(N) KEGG pathway enrichment analysis of genes increased in FTD versus Ctrl. Representative members of select pathway cluster are shown. The x and y axes show the normalized enrichment values and the negative $\log_{10}$ of the adjusted *p* value, respectively. The adjusted *p* value and number of genes are also denoted by color and by size, respectively.

Scale bars: 2 mm (A), 100 μm (left images in D, G, and J), and 50 μm (right images in D, G, and J). $^*p < 0.05$, $^{**}p < 0.01$, $^{***}p < 0.001$, $^{****}p < 0.0001$—two-tailed Student's t test. Data are presented as mean + SEM.

SLC6A1, and *MEIS2* in Neuron_Inh (Figure 2I). These clusters were not equally distributed between the Ctrl and FTD groups, as Neuron_DA and Neuron_CALB2 were relatively depleted from FTD cases (Figure 2H). These differences are also reflected in pseudotime analyses on nigral Ctrl and FTD neurons (Figures S1E–S1G).

iPSC-derived FTD neurons demonstrate tau pathology and heightened oxidative phosphorylation

We next modeled FTD *in vitro* using human iPSC-derived neuronal cultures. We used independent iPSC clones from FTD patients carrying *MAPT-N279K* (FTD-1 and FTD-2) or *MAPT-V337M* (an FTD-associated, pathogenic *MAPT* mutation located in exon 12; FTD-3),[20] as well as independent iPSC clones from healthy Ctrl individuals (Ctrl-1, Ctrl-2, and Ctrl-3) or gene-corrected, isogenic control cells (FTD-1-GC and FTD-2-GC).[21] Neurons were differentiated through an intermediate of neural progenitor cells (NPCs) as previously described[22–24] (Figures S2A and S2B). Differentiated neurons showed expression of the neuronal protein beta-III tubulin (TUJ1; Figures 3A and 3B) and the synaptic vesicle protein-2 (SV-2; Figure 3C). A subset of neurons expressed TH (Figure 3A), and another population was positive for GABA (Figure 3B). There were no significant differences in the proportions of TH+ and GABA+ neurons between FTD and Ctrl (Figures S2C and S2D). However, cultures composed of FTD

Please cite this article in press as: Al-Dalahmah et al., Osteopontin drives neuroinflammation and cell loss in *MAPT-N279K* frontotemporal dementia patient neurons, Cell Stem Cell (2024), https://doi.org/10.1016/j.stem.2024.03.013

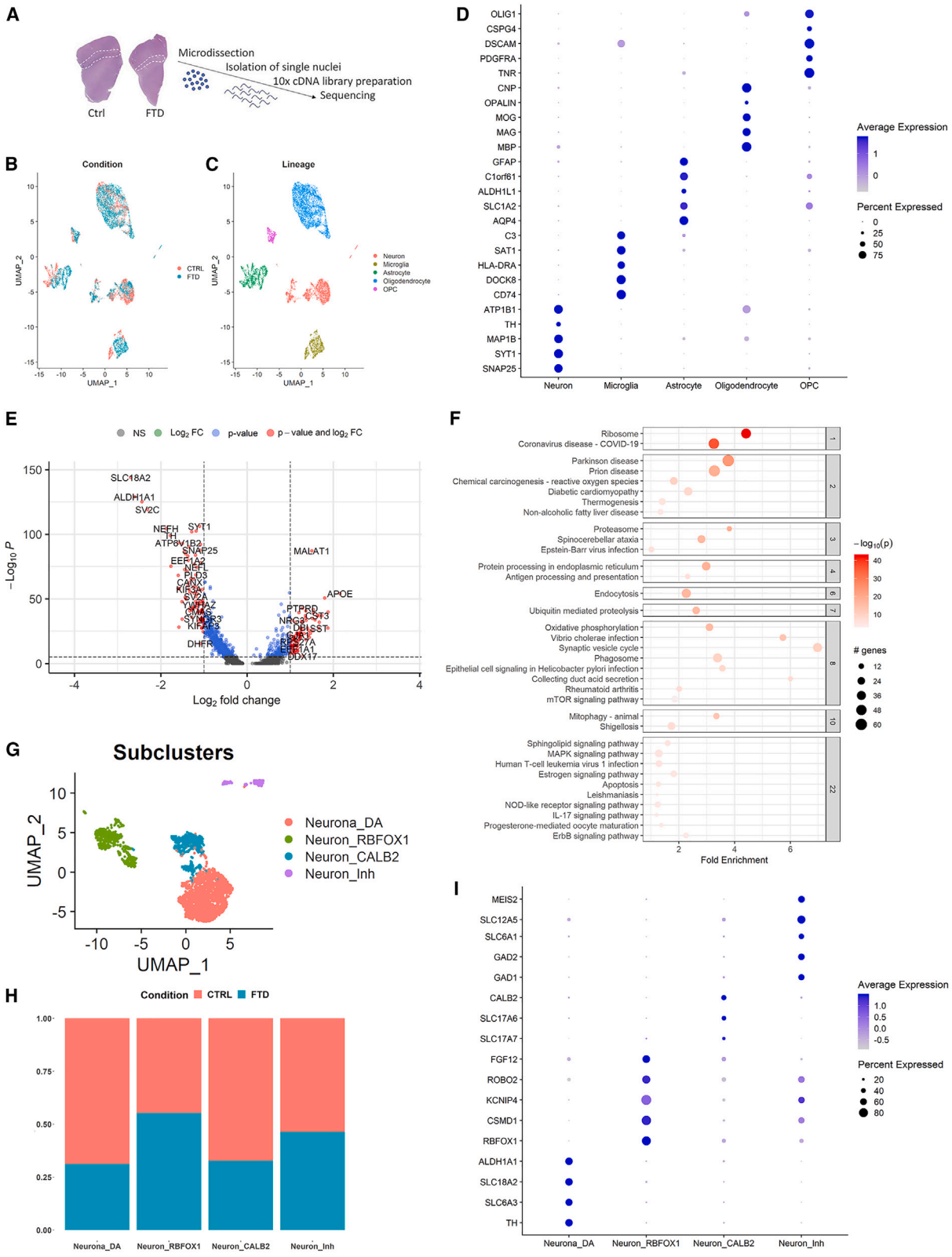

Figure 2. Transcriptional pathology in nigral FTD neurons

(A) Cartoon illustration of the study design.

(B) UMAP plots of FTD and Ctrl nuclei color-coded by condition.

(legend continued on next page)

Please cite this article in press as: Al-Dalahmah et al., Osteopontin drives neuroinflammation and cell loss in *MAPT-N279K* frontotemporal dementia patient neurons, Cell Stem Cell (2024), https://doi.org/10.1016/j.stem.2024.03.013

cells contained an increased number of p-tau+ (AT8+) neurons (Figures 3D and 3E) and showed an increased expression of 4R tau isoforms in the context of high 3R tau isoform expression (FTD-1 and FTD-2; Figures S2E and S2F). Furthermore, FTD neurons exhibited increased vulnerability toward oxidative stress induced by rotenone, oligomycin, and antimycin A, which block mitochondrial complexes I, V, or III, respectively (Figure 3F), and they showed impaired mitophagy (Figures S2G–S2J).

We next focused on oxidative phosphorylation, one of the major pathways enriched in postmortem FTD neurons (Figure 2F). We measured the oxygen consumption rate (OCR) at baseline and under different conditions including rotenone, oligomycin, and antimycin A using the Seahorse assay (Figures 3G–3I and S2K–S2M). FTD neurons from all iPSC lines demonstrated an elevated basal respiration, ATP production, maximal respiratory capacity, and spare respiratory capacity when compared with Ctrl neurons (Figures 3G–3I and S2K–S2M). These findings were also seen when we introduced the *MAPT-P301L* mutation, another FTD-causing genetic alteration, as heterozygous or homozygous mutations in healthy Ctrl cells (Figures S2N–S2P). Overexpression of *wt-MAPT* in FTD neurons as well as *MAPT* knockdown (KD) in healthy Ctrl neurons did not change oxygen consumption (Figures S2R, S2S, S2U, and S2V), demonstrating that OCR is not dependent on *MAPT* levels in iPSC-derived neurons and that increased OCR in FTD neurons was not due to loss of *MAPT* function. By contrast, the different OCR parameters were normalized in FTD neurons when we genetically corrected the *MAPT-N279K* mutation (Figures 3G–3I and S2K–S2M). We also found that increased oxidative phosphorylation in FTD neurons was chemically targetable, as the application of metformin, an FDA-approved anti-diabetic drug and inhibitor of complex I, almost completely normalized cellular respiration in a manner akin to Ctrl neurons (Figure 3J). Metformin also led to significant changes in the transcriptome profile in FTD neurons with a negative enrichment of those DEGs that were upregulated in neurons in postmortem FTD brains (Figure 3K).

We next performed mass spectrometry for about 150 polar metabolites associated with the intermediary metabolism (Figures 3L–3Q; Table S3). FTD neurons showed strong elevation of numerous metabolic substrates associated with glycolysis (pyruvic acid), tricarboxylic acid (TCA) cycle (fumaric acid and malic acid), and nucleotide synthesis (aspartic acid), indicating an elevated catabolic state in FTD neurons (Figure 3L). In support of this observation, FTD neurons contained significantly increased levels of ATP (Figure 3M). A metabolomics enrichment analysis identified dysregulated pathways linked, among others, to mitochondrial electron transport chain, pyruvate metabolism, and metabolism of amino acids (Figure 3N).

We performed ^{13}C carbon tracing analyses to address the question of whether FTD neurons utilize the major energy fuels, glucose, amino acids, and fatty acids differently, compared with Ctrl cells, accounting for the heightened energy state and ATP production in FTD neurons (Figures 3O–3Q and S2X–S2Z′; Table S3). Either ^{13}C-glucose, ^{13}C-glutamine, or ^{13}C-palimitic acid was applied to FTD and Ctrl neurons for 24 h, and mass spectrometry for polar metabolites was performed to identify ^{13}C-labeled carbon molecules within these metabolites as derivatives of the ^{13}C-labeled energy source (exemplified for ^{13}C-labeled glucose as energy fuel in Figure 3O). Glucose is the main energy source in neurons and reacts to pyruvate in glycolysis feeding into the TCA cycle for ATP production (Figure 3O). We found that more glucose carbons incorporated into TCA cycle intermediates in FTD neurons such as citric acid, oxoglutaric acid, and malic acid, indicating an increased utilization of glucose for oxidative energy production in FTD neurons (Figures 3P and S2X). Likewise, the application of ^{13}C-labeled glutamine resulted in an increased incorporation of ^{13}C in the TCA cycle intermediates citric acid and fumaric acid, highlighting that also amino acids are utilized at much higher levels in FTD neurons for ATP production (Figures 3Q and S2Y). While the utilization of fatty acids was very low in both FTD or Ctrl neurons, we found minimally reduced utilization of palmitic acid in neurons from one but not another FTD iPSC line (Figures S2Z and S2Z′), suggesting that beta-oxidation of fatty acids is not a significant source of energy production in FTD versus Ctrl neurons. Overall, these carbon tracing results demonstrate that elevated oxidative phosphorylation in FTD neurons is related to increased utilization of glucose and amino acids but not fatty acids.

FTD iPSC neurons carry a pro-inflammatory signature

Our snRNA-seq analyses on postmortem nigral tissue revealed an enrichment of inflammatory pathways in FTD neurons (Figure 2F). Thus, we next asked if the pro-inflammatory signature could be modeled in iPSC-derived neurons. We first characterized gene expression profiles and found that 2,260 genes were significantly upregulated and that 1,821 genes were significantly downregulated in FTD neurons (Figures S3A–S3C). 55 of the increased and 159 of the decreased DEGs were shared with postmortem FTD neuronal DEGs measured by snRNA-seq (Figure S3A). KEGG pathway enrichment analysis identified pro-inflammatory pathways including human T cell leukemia virus 1 infection, tumor necrosis factor (TNF) signaling, T helper (Th) 17 cell differentiation, and IL-17 signaling to be enriched in iPSC-derived and postmortem FTD neuronal DEGs (Figure S3C; Table S2). A subset of the DEGs is presented in a heatmap in Figure S3B demonstrating decreased expression of the dopaminergic marker *TH* and elevated expression of the

(C) UMAP plot of FTD and Ctrl neuronal nuclei color-coded by lineage. OPC, oligodendrocyte precursor cell.
(D) Dot plot graph showing the expression of lineage-associated genes.
(E) Volcano plot showing DEGs between FTD and Ctrl donor neurons.
(F) KEGG pathway enrichment analysis of the genes increased in FTD neurons. The plot is generated as in Figure 1N.
(G) UMAP plot highlighting four neuronal subclusters (DA, RBFOX1, CALB2, and Inh).
(H) Relative distribution of the four neuronal subclusters in the FTD and Ctrl groups.
(I) Dot plot graph showing the expression of signature genes.
See also Figure S1.

Please cite this article in press as: Al-Dalahmah et al., Osteopontin drives neuroinflammation and cell loss in *MAPT-N279K* frontotemporal dementia patient neurons, Cell Stem Cell (2024), https://doi.org/10.1016/j.stem.2024.03.013

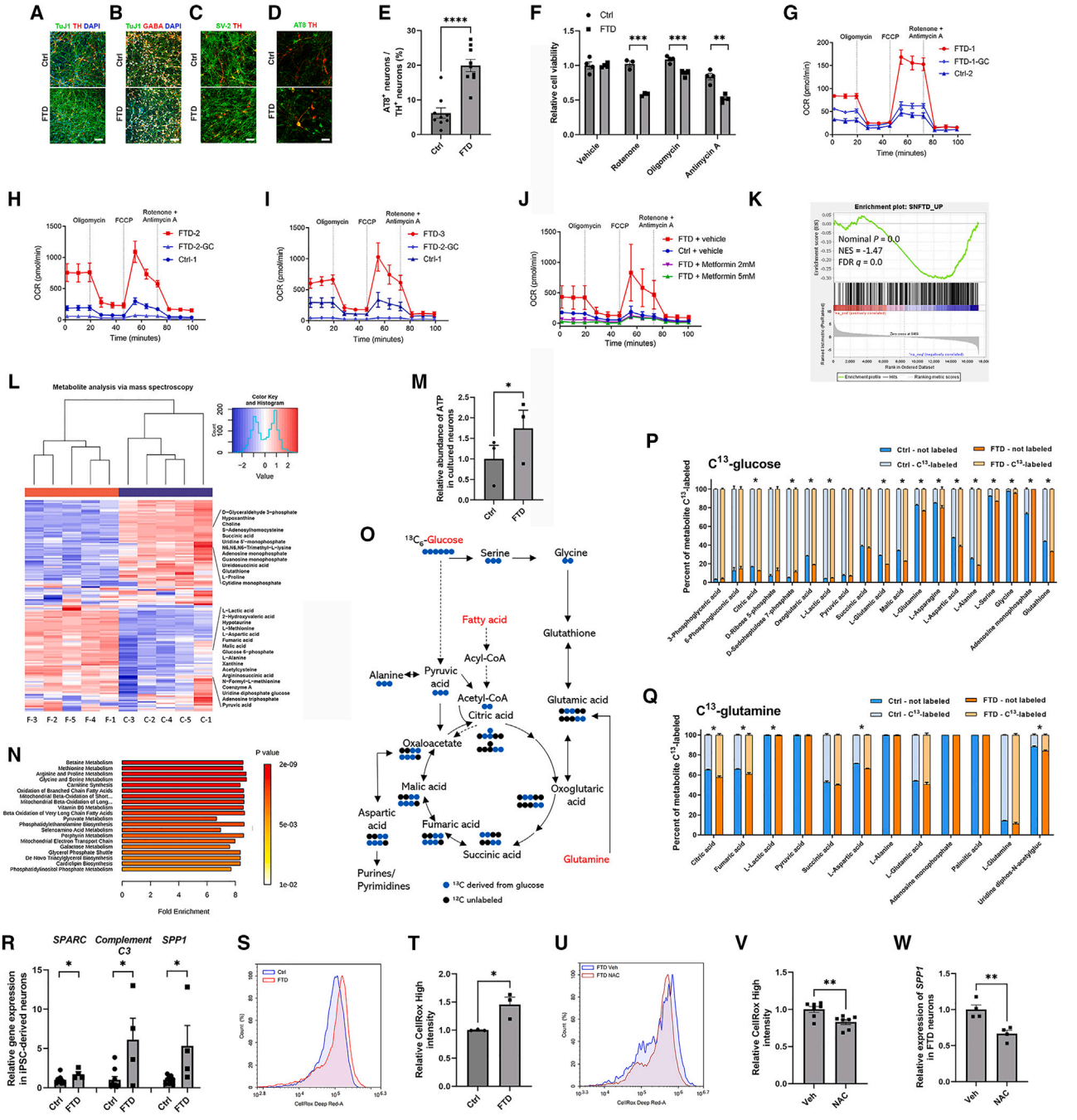

Figure 3. FTD patient iPSC-derived neurons show tau pathology and increased oxidative stress, cellular respiration, and neuroinflammation

(A) Immunostainings for TUJ1 and TH.

(B) Immunostainings for TUJ1 and GABA.

(A and B) Nuclei are labeled with DAPI.

(C) Immunostainings for TH and SV-2.

(D) Immunostainings for TH and AT8.

(E) Quantification of AT8^{+} DA neurons in neuronal cultures.

(F) MTS assay with rotenone (200 nM), oligomycin (10 nM), and antimycin A (5 nM).

(G–I) Seahorse assays for different FTD and Ctrl iPSC clones.

(J) Seahorse assay demonstrating the rescue of increased respiration by metformin.

(K) Enrichment plot showing that metformin treatment in FTD iPSC neurons leads to the depletion of DEGs upregulated in neurons in postmortem FTD brains.

(L) Heatmap showing the mass spectrometry expression data for about 150 polar metabolites in FTD versus Ctrl neurons.

(legend continued on next page)

Please cite this article in press as: Al-Dalahmah et al., Osteopontin drives neuroinflammation and cell loss in *MAPT-N279K* frontotemporal dementia patient neurons, Cell Stem Cell (2024), https://doi.org/10.1016/j.stem.2024.03.013

inflammation-associated genes *C3* (complement factor 3; a known microglial activator[25]), *SPARC*, and *SPP1* (secreted phosphoprotein 1 or osteopontin [OPN]) in FTD iPSC-derived neurons, as also verified by RT-qPCR (Figure 3R). The latter two genes were shared with postmortem FTD neurons by snRNA-seq (Figure S1D). Furthermore, *in situ* hybridization revealed an increased expression of *C3*, *SPARC*, and *SPP1* in postmortem FTD neurons (Figures S3D–S3G).

The enrichment of pro-inflammatory genes in FTD neurons led us to investigate whether it is related to increased production of reactive oxygen species (ROS) since ROS production can facilitate a pro-inflammatory response.[26] Our snRNA-seq data on postmortem FTD neurons show an enriched ROS signature (Figure 2F), and previous reports have demonstrated increased levels of ROS in neurons carrying *MAPT* mutations.[27,28] Thus, we measured ROS production in our cultured FTD and Ctrl neurons using the CellRox flow cytometry assay (Figures 3S and 3T). FTD neurons showed higher levels of ROS (Figures 3S, 3T, and S3H–S3J), which could be reduced after application of the ROS-blocking compound N-acetyl-cystein (NAC; Figures 3U, 3V, and S3K). To test if the increased expression of the pro-inflammatory genes *C3*, *SPARC*, and *SPP1* in FTD neurons could be reduced by blocking ROS, we next measured their expression after application of NAC (Figures 3W, S3L, and S3M). We found significant downregulation of *SPP1* but unaltered levels of *C3* and *SPARC* in the presence of NAC, indicating that ROS differentially modulates the expression of these pro-inflammatory genes in FTD neurons with downstream regulation of *SPP1*.

We next wondered if the pro-inflammatory signature in FTD neurons could mediate effects on cultured microglia leading to an altered microglial response *in vitro*. First, we identified alterations in postmortem FTD microglia in snRNA-seq results (Figures 4A–4E). Projecting only microglial nuclei in their own UMAP space revealed FTD and Ctrl microglia to occupy largely non-overlapping regions (Figure 4A). Subclustering the microglial nuclei demonstrated three subclusters, two of which were largely composed of FTD nuclei and showed separation along a pseudotime trajectory axis (Figures 4B, 4C, S1H, and S1I). A subset of the gene markers of each subcluster is shown in Figure 4D, and the full list is in Table S4. Subcluster Micro_0_FTD demonstrated upregulation of markers of reactivity, such as *CD68*, antigen presentation machinery genes *CD74* and *B2M*, pro-phagocytic function like *CD14* and *TYROBP*—binding partner of TREM2, and *APOE* (Figure 4D; Table S4). Subcluster Micro_1_FTD demonstrated expression of monocyte markers like *PTPTRC* (CD45) and *IRAK3*. The Ctrl cluster Micro_2_CTRL demonstrated expression of baseline microglial genes like *CX3CR1* and *P2RY12* (Figure 4D; Table S4). Differential gene expression analysis between Ctrl and FTD microglia revealed 707 DEGs (Table S4), 214 of which were increased including *MITF*, *GPNMB*, *APOE*, *CD74*, Ferritin light chain gene (*FTL*), complement genes *C1QA* and *C1QB*, *CD9*, *ITM2B*, *CEBPD*, and *CXCR4* (Figure 4E), as well as the pro-phagocytic genes *TYROBP* and *TREM2* (Table S4). These results showed that FTD microglia adopt a reactive, pro-phagocytic phenotype.

Next, we asked if specific factors in FTD neuronal-conditioned media lead to microglial activation. We focused on OPN as one of the factors that we had identified in our transcriptomics studies on postmortem brains (bulk and snRNA-seq neurons) and iPSC neurons and by *in situ* hybridization on patient brain tissue. Measurement of secreted OPN in the medium of FTD and Ctrl neurons through ELISA revealed about a 2-fold increase in the FTD group (Figure 4F). Application of the FTD neuron-conditioned medium to human microglial HMC-3 cells resulted in increased phagocytosis, which was significantly reduced by adding an OPN-blocking antibody to the medium (Figures 4G and S3N), indicating a potential role of OPN in modulating microglial responses.

To test if OPN alters FTD-associated transcriptional programs in human microglia, we differentiated Ctrl and FTD iPSCs with the *MAPT-N279K* mutation into induced microglial cells (iMGLs) using an established protocol.[29] FTD and Ctrl iPSCs showed similar differentiation capabilities with about 90% Iba-1$^+$ microglia in cultures of different FTD and Ctrl lines (Figures 4H, 4I, S3O, and S3P). FTD and Ctrl iMGLs responded similarly toward the pro-inflammatory molecule LPS (lipopolysaccharide) with a strong upregulation of *TNF* and *IL1b* (Figures S3Q and S3R), indicating that both FTD and Ctrl microglia were responsive to inflammatory cues and could be activated *in vitro*. We then compared the expression of selected FTD-associated microglial DEGs (Table S4) in FTD and Ctrl iMGLs at baseline and found, except for CD74, similar levels of *TREM2*, *MITF*, *GPNMB*, *CXCR4*, *APOE*, *C1QA*, *C1QB*, *CD9*, *FTL*, *CEBPD*, and *ITM2B* in both groups (Figure S3S). In addition, *TNF* was similarly expressed in FTD and Ctrl iMGLs. We then tested the effects of OPN on the expression of the same set of genes in FTD and Ctrl iMGLs and found that OPN increased the levels of *TNF*, *MITF*, *GPNMB*, and *CXCR4* in both groups (Figure 4J). In addition, FTD iMGLs upregulated *CD74* and the complement genes *C1QA* and *C1QB* upon OPN treatment, which was not seen in

(M) Quantification of ATP in FTD and Ctrl neurons.
(N) Top 20 metabolomics pathways enriched in FTD neurons.
(O) Schematic presentation of the intermediary metabolism with glucose, glutamine, and fatty acids as energy fuels (in red). Shown are unlabeled ^{12}C-glucose carbons (black) and ^{13}C-glucose carbons (blue) and how the latter are transferred among molecules of the TCA cycle.
(P) Percentages of selected ^{13}C-labeled and ^{12}C-unlabeled metabolites after application of ^{13}C-glucose to the medium of FTD and Ctrl neurons.
(Q) Percentages as described for (P), but after the application of ^{13}C-glutamine.
(R) RT-qPCR for *SPARC*, *C3*, and *SPP1*.
(S) Flow cytometry of FTD and Ctrl neurons using the CellRox assay to measure ROS production.
(T) Quantification of relative ROS production in FTD and Ctrl neurons.
(U) Flow cytometry of FTD neurons to measure ROS production in the presence of absence of NAC using the CellRox assay.
(V) Quantification of relative ROS production in vehicle- or NAC-treated FTD neurons.
(W) RT-qPCR for *SPP1* in vehicle- or NAC-treated FTD neurons.
Scale bars: 100 μm (A and B), 50 μm (C), and 25 μm (D). $^*p < 0.05$, $^{**}p < 0.01$, $^{***}p < 0.001$, $^{****}p < 0.0001$—two-tailed Student's t test (E, F, R, T, V, and W) or multiple t test (P and Q). Data are presented as mean + SEM (+ SD in P and Q). See also Figures S2 and S3.

Please cite this article in press as: Al-Dalahmah et al., Osteopontin drives neuroinflammation and cell loss in *MAPT-N279K* frontotemporal dementia patient neurons, Cell Stem Cell (2024), https://doi.org/10.1016/j.stem.2024.03.013

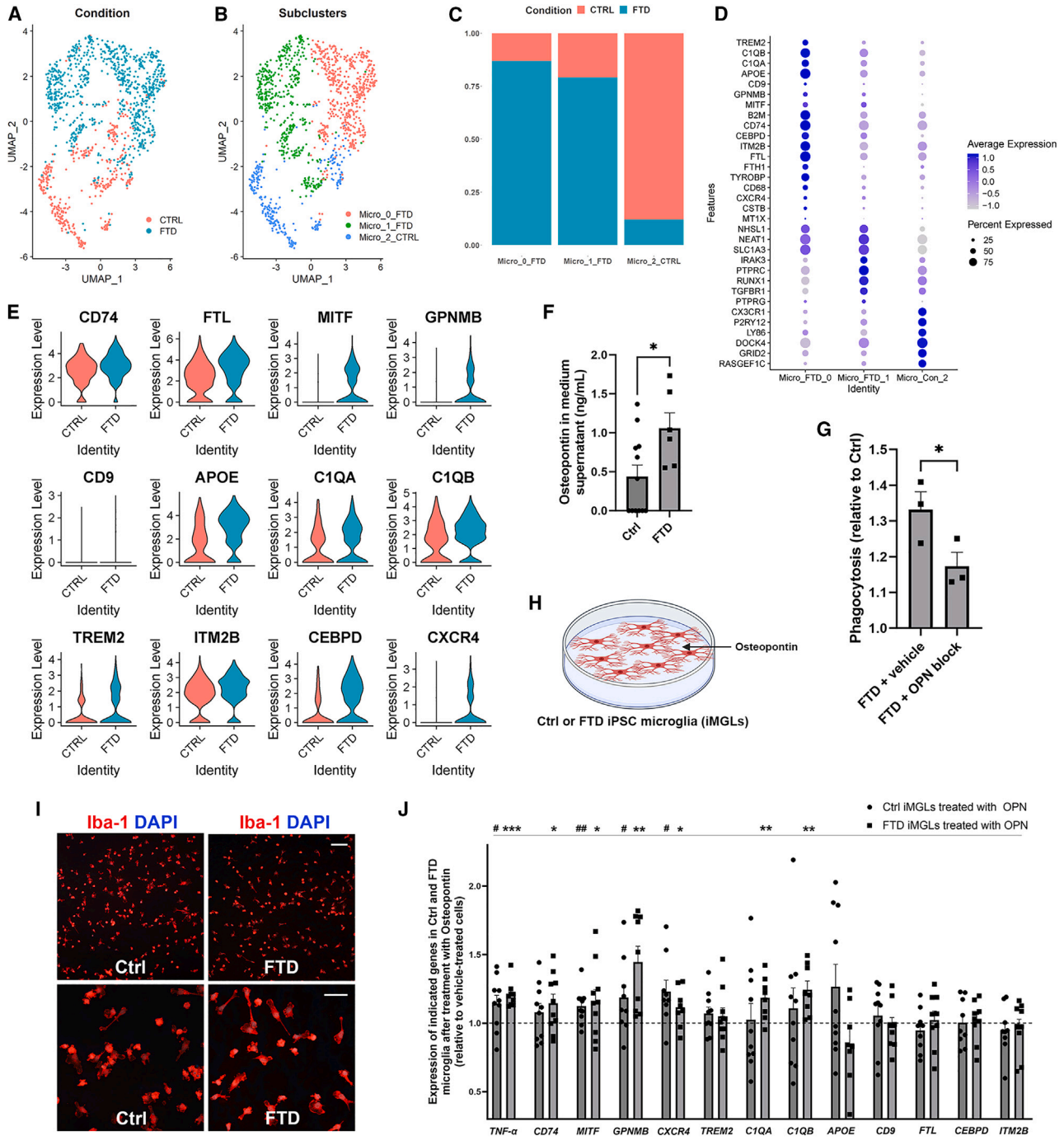

Figure 4. Transcriptional pathology in postmortem FTD microglia and in cultured microglia after application of osteopontin

(A) UMAP plot of postmortem FTD and Ctrl microglial nuclei color-coded by condition.

(B) As in (A), but color-coded by microglial subclusters.

(C) Relative distribution of the three microglial subclusters in FTD and Ctrl microglia.

(D) Dot plot graph showing the expression of most upregulated genes within the three microglial subclusters.

(E) Violin plots of significantly upregulated genes in FTD microglia.

(F) ELISA of the medium supernatant of cultured Ctrl or FTD neurons for osteopontin.

(G) Relative phagocytosis in microglial cell line (HMC-3) cultured in conditioned medium of FTD neurons in the presence or absence of an osteopontin-blocking antibody.

(H) Schematic drawing of the culture of human Ctrl and FTD iPSC-derived induced microglial cells (iMGLs) with treatment with osteopontin.

(I) Immunostainings of Ctrl and FTD iMGLs for Iba-1 with DAPI counterstaining. Scale bars: 100 μm for low-power images (top) and 50 μm for higher-power images (bottom).

(legend continued on next page)

Please cite this article in press as: Al-Dalahmah et al., Osteopontin drives neuroinflammation and cell loss in *MAPT-N279K* frontotemporal dementia patient neurons, Cell Stem Cell (2024), https://doi.org/10.1016/j.stem.2024.03.013

Ctrl microglia (Figure 4J). These findings demonstrated a similar, yet differential, response of FTD and Ctrl microglia toward OPN.

Transplantation of FTD iPSC neural cells into the brains of mice results in decreased neuronal survival and increased microglial infiltration

To study the pathology of FTD neurons in a three-dimensional, physiological environment and to interrogate further a potential role of FTD neurons on a microglial response, we next transplanted FTD or Ctrl iPSC-derived NPCs into the forebrain of NSG (NOD.Cg-Prkdc scid Il2rg tm1Wjl/SzJ) mice (Figure 5A). 4 months after cell injection, brains were examined histologically demonstrating viable neuronal grafts in all animals of both groups without tissue overgrowth (Figures 5B–5H). However, grafts composed of FTD neurons were significantly smaller and contained fewer surviving neurons, which we quantified in immunostainings for human nuclear antigen (HNA) and NeuN as well as with *in situ* hybridizations for synaptophysin (Figures 5B–5F and S4A–S4D). Engrafted neurons expressed the neural cell adhesion molecule hNCAM (Figure 5G) as well as the synaptic markers synaptophysin (Figure 5H) and SV-2 (Figure S4E). By using a human-specific NCAM antibody, the growth of transplanted Ctrl and FTD neurons in the mouse brains could be readily visualized. Human neurons sent $hNCAM^+$ axonal projections directly into the adjacent striatum and to remote areas along white matter tracts, which appeared reduced in the FTD group secondary to neuronal loss (Figure 5G). A few iPSC-derived $hGFAP^+$ astrocytes were also present in FTD and Ctrl grafts, but there was no difference in hGFAP-positivity between the groups (Figures S4F and S4G). iPSC-derived oligodendrocytes were not seen in the grafts (Figure S4H).

We next examined the host microenvironment within and adjacent to the FTD and Ctrl neuronal grafts (Figures 5I–5N). Immunostainings for GFAP highlighted an increased astroglial reactivity within and adjacent to the FTD grafts (Figures 5I, 5J, 5L, and 5M). Immunostainings for Iba-1 demonstrated pronounced microglial activation in the graft center and at the graft edge in the FTD group with significantly increased numbers of $Iba\text{-}1^+$ microglia in both areas (Figures 5I, 5K, 5L, and 5N). These findings showed that FTD neurons promote a neuroinflammatory response *in vivo*, further confirming and expanding on our previous observation of a pro-inflammatory signature in FTD neurons in culture and in postmortem human brains. Notably, this glial reaction was paralleled by a significantly reduced number of surviving host (murine) neurons ($NeuN^+/HNA^-$) within the FTD grafts (Figures 5O and 5P), further highlighting a detrimental effect of engrafted FTD neurons on the microenvironment.

To investigate the pathological changes in engrafted FTD neurons and in host glial cells at a single-cell level, we microdissected FTD and Ctrl grafts and performed snRNA-seq, capturing both engrafted human cells and host cells (Figures 6A and 6B). Overall, we captured 35,885 murine nuclei (17,116 and 18,769 nuclei within and right adjacent to Ctrl or FTD grafts) and 5,974 human nuclei (4,391 from Ctrl and 1,583 from FTD grafts). The human population was mainly composed of neurons in both FTD and Ctrl grafts (Figures 6C and 6D). FTD grafts yielded fewer neuronal nuclei, while a similarly small number of human astrocytes was found in the FTD and Ctrl groups (Figures 6C and 6D). In addition, a small number of human NPCs was found mainly in the FTD group. Notably, there was a clear separation within the neuronal and astrocytic clusters when comparing the FTD and Ctrl groups in the UMAP plot (Figures 6C and 6D). We investigated the KEGG pathways that were enriched in the DEGs between FTD and Ctrl graft neurons (Figure 6E; Table S5). Pathways involved oxidative phosphorylation, neurodegeneration (PD), and inflammatory response (Salmonella infection, Yersinia infection, antigen presentation) were significantly increased in transplanted FTD neurons, as similarly observed in cultured iPSC-derived and postmortem FTD neurons.

We next asked if engrafted FTD iPSC neurons resembled their postmortem counterparts, with the caveat that the former are young neurons while the latter have aged for several decades. We thus correlated normalized gene expression between postmortem and graft neurons and found that the correlation between FTD postmortem and engrafted FTD neurons was high and that the correlation between Ctrl engrafted and Ctrl postmortem neurons was relatively low (Figure 6F). To further establish this finding, we scored the graft neurons by the expression of the genes that were significantly increased in postmortem FTD neurons and found the FTD graft neurons showed significantly higher scores of the postmortem FTD neuronal signature (Figure 6G). Furthermore, when we aligned the graft and postmortem neuronal datasets, FTD graft neurons and postmortem neurons colocalized in the UMAP space, but the Ctrl graft and postmortem neurons did not (Figure 6H).

We wondered if host murine microglia were also correlated with postmortem microglia. After identifying the major cell types in the murine population, neurons, astrocytes, oligodendrocytes, endothelial cells, and microglia (Figure 6I), we tested if mouse microglia within and around FTD grafts carry a reactive gene signature. A higher percentage of murine microglia carried a transcriptional signature of reactive microglia in the FTD group compared with the Ctrl group (Figures 6J and S4I), with separation along a pseudotime trajectory axis (Figures S4J and S4K), confirming our previous results of increased microglial reactivity by histology. We then performed correlation studies of normalized transcriptome profiles between mouse microglia and human postmortem microglia in the FTD and Ctrl groups. The results showed that the two populations were more highly correlated with one another in FTD when compared with Ctrl (Figure 6K). Scoring the host microglia by the expression of the genes that were significantly increased in postmortem FTD microglia revealed significantly higher scores of the postmortem FTD-microglial signature in the murine microglia adjacent to FTD neurons (Figure 6L). Together, the results showed that grafted FTD neurons lead to activation of microglia with an FTD-associated transcriptional signature.

(J) RT-qPCR demonstrating the relative expression of *TNF* and of indicated FTD microglia-associated DEGs in cultured osteopontin-treated Ctrl (Ctrl-4, Ctrl-5, and Ctrl-6) and FTD (FTD-4, FTD-5, and FTD-6) iMGLs relative to vehicle-treated Ctrl and FTD iMGLs, respectively.
$^*p < 0.05$—two-tailed Student's t test (F and G). $^{\#}p < 0.05$ and $^{\#\#}p < 0.01$ (Ctrl iMGLs) and $^*p < 0.05$, $^{**}p < 0.01$, and $^{***}p < 0.001$ (FTD iMGLs)—one-tailed one-sample t test (J). Data are presented as mean + SEM. See also Figures S1 and S3.

Please cite this article in press as: Al-Dalahmah et al., Osteopontin drives neuroinflammation and cell loss in *MAPT-N279K* frontotemporal dementia patient neurons, Cell Stem Cell (2024), https://doi.org/10.1016/j.stem.2024.03.013

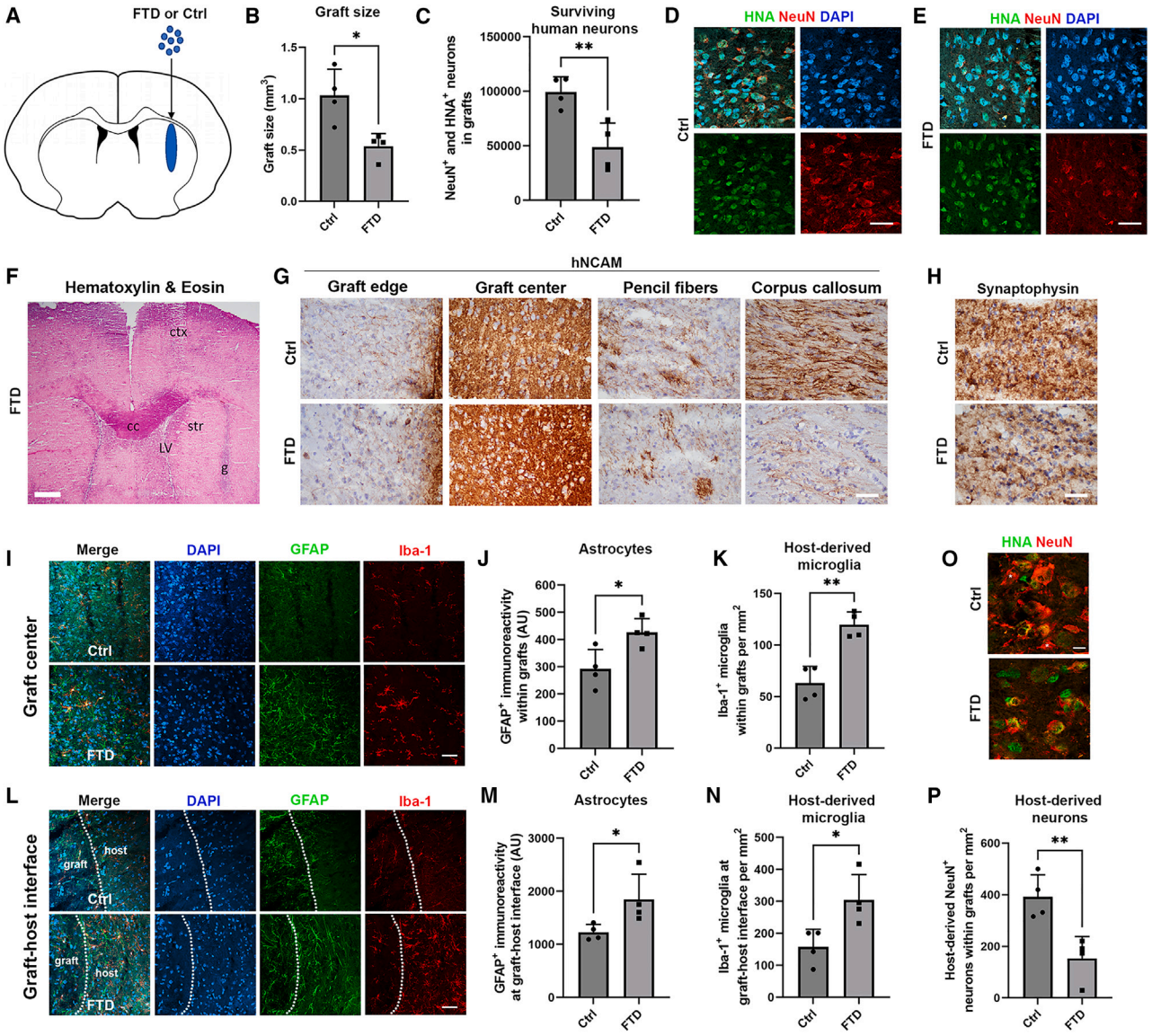

Figure 5. Transplantation of FTD and Ctrl neural cells into the brains of adult mice

(A) Schematic drawing of the injection of FTD and Ctrl NPCs into the mouse brain.
(B) Quantification of the size of grafts.
(C) Quantification of surviving neurons in grafts.
(D) Immunostainings of Ctrl grafts for human nuclear antigen (HNA) and NeuN.
(E) Immunostainings of FTD grafts for HNA and NeuN.
(F) H&E-stained section of a mouse brain with an FTD graft. LV, lateral ventricle; ctx, cortex; cc, corpus callosum; str, striatum; g, graft.
(G) Immunostainings of grafts for human NCAM.
(H) Immunostainings of grafts for synaptophysin.
(I) Immunostainings of the center of grafts for GFAP and Iba-1.
(J) Quantification of GFAP signal intensity within grafts.
(K) Quantification of host microglia within grafts.
(L) Immunostainings of the graft-host interface for GFAP and Iba-1.
(D, E, I, and L) Nuclei are labeled with DAPI.
(M) Quantification of GFAP signal intensity at the graft-host interface in the FTD and Ctrl groups.
(N) Quantification of host microglia at the graft-host interface in the FTD and Ctrl groups.
(O) Immunostainings of grafts for HNA and NeuN with high-power view showing $HNA^+/NeuN^+$ grafted neurons and $HNA^-/NeuN^+$ host neurons.
(P) Quantification of $HNA^-/NeuN^+$ host neurons within grafts.
Scale bars: 20 μm (D and E), 500 μm (F), 50 μm (G, H, I, and L), and 10 μm (O). $^*p < 0.05$ and $^{**}p < 0.01$—two-tailed Student's t test. Data are presented as mean + SEM. See also Figure S4.

Please cite this article in press as: Al-Dalahmah et al., Osteopontin drives neuroinflammation and cell loss in *MAPT-N279K* frontotemporal dementia patient neurons, Cell Stem Cell (2024), https://doi.org/10.1016/j.stem.2024.03.013

CellPress
OPEN ACCESS

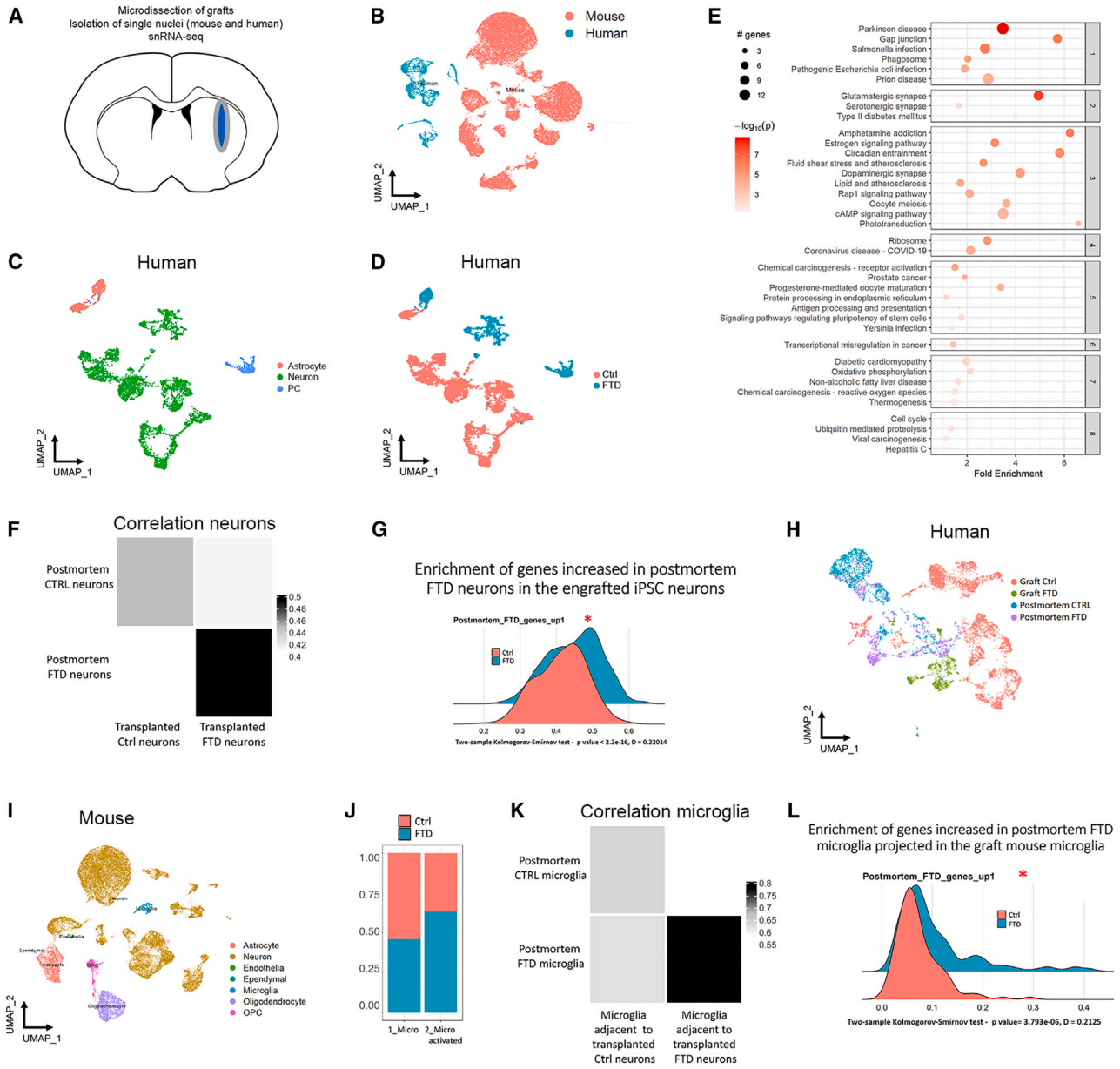

Figure 6. snRNA-seq of microdissected FTD and Ctrl grafts

(A) Schematic drawing of the experimental approach.

(B) UMAP plot of nuclei from microdissected FTD and Ctrl grafts color-coded by species.

(C) UMAP plot of human nuclei color-coded by lineage.

(D) As in (C), but color-coded by condition.

(E) KEGG pathway enrichment analysis of the genes increased in grafted FTD neurons. The plot is generated as in Figure 1N.

(F) Heatmap showing the Pearson correlation coefficients between transplanted FTD neurons, transplanted Ctrl neurons, postmortem FTD neurons, and postmortem Ctrl neurons.

(G) Histograms showing the enrichment scores of genes increased in postmortem FTD neurons demonstrated in engrafted FTD and Ctrl iPSC-derived neurons.

(H) UMAP plots of grafted FTD and Ctrl neurons and of postmortem FTD and Ctrl neurons color-coded by group.

(I) UMAP plot of mouse nuclei within and adjacent to microdissected grafts color-coded by cell type.

(J) Proportion of resting and activated mouse microglia within and adjacent to grafts.

(K) As in (F), but for mouse microglia within and adjacent to FTD and Ctrl grafts, postmortem FTD and Ctrl microglia.

(L) As in (G), but for genes increased in postmortem microglia projected in host murine microglia.

Two-sample Kolmogorov-Smirnov test was applied in (G) and (L). The *p* values are indicated. See also Figure S4.

Please cite this article in press as: Al-Dalahmah et al., Osteopontin drives neuroinflammation and cell loss in *MAPT-N279K* frontotemporal dementia patient neurons, Cell Stem Cell (2024), https://doi.org/10.1016/j.stem.2024.03.013

Downregulation of OPN in FTD neurons results in increased engraftment and in reduced microglial infiltration after cell transplantation into the mouse brain

Given the increased expression of OPN/*SPP1* in FTD neurons and OPN-mediated effects on human microglia *in vitro*, we wondered if increased vulnerability of FTD neurons was related to elevated expression of OPN/*SPP1*, either directly or indirectly through a neuroinflammatory response or both. To address this question, we first investigated if OPN/*SPP1* by itself is sufficient to elicit a pro-inflammatory phenotype in Ctrl neurons. When we compared gene expression profiles in iPSC neurons overexpressing *SPP1* ($Ctrl^{SPP1}$) versus GFP ($Ctrl^{GFP}$) by RT-qPCR and bulk RNA-seq, we found that overexpression of *SPP1* did not influence the expression of *SPARC* and *C3* (Figure S5A). In fact, besides *SPP1*, only four other genes (*NBPF20*, *ATP1A3*, *DCLRE1B*, and *H3P6*) were significantly differentially expressed after *SPP1* overexpression, which are not associated with neuroinflammation (Table S6). We then transplanted $Ctrl^{SPP1}$ or $Ctrl^{GFP}$ NPCs into the forebrain of NSG mice and examined the grafts 2 weeks later (Figure S5B). While $Ctrl^{GFP}$ grafts were composed of $hNCAM^+$ cells and contained some areas with necrotic cells and microglial infiltration secondary to the injection, the grafts composed of $Ctrl^{SPP1}$ cells did not survive (Figure S5C). Instead, pronounced microgliosis was seen at the injection site with a significantly higher number of Iba-1^+ microglia in the $Ctrl^{SPP1}$ group (Figures S5D–S5F). These results demonstrated that *SPP1* on its own is sufficient to drive host microglial reactions *in vivo*.

We next asked if KD of *SPP1* in FTD neurons reduces the pro-inflammatory gene signature that we had observed in FTD neurons. We first compared gene expression profiles in FTD neurons transduced with shRNAs to downregulate *SPP1* expression (FTD^{shSPP1}) versus scrambled shRNA as control (FTD^{scr}). RT-qPCR validated the *SPP1* KD in FTD neurons and demonstrated a significantly reduced expression of *SPARC* but not of *C3* (Figure 7A). These initial findings indicated that, in contrast to Ctrl neurons, expression of *SPARC* is dependent on *SPP1* levels in FTD neurons. We next performed bulk RNA-seq on FTD neurons with or without *SPP1* KD and found that 2,592 genes were significantly differentially expressed, 1,407 of which were decreased in FTD^{shSPP1} (Table S6). Interestingly, downregulated transcripts included inflammation-associated genes such as *IL17RB*, *IL17RC*, *IL2RB*, *IL4R*, *CXCR4*, and *CXCL12* (Table S6). We performed active subnetwork KEGG pathway enrichment analysis and found that many inflammation-related pathways were significantly enriched in the genes decreased in FTD neurons after *SPP1* KD, including JAK-STAT, nuclear factor κB (NF-κB), and IL-17 signaling as well as other inflammation-related pathways (Table S6). Moreover, multiple genes and pathways involved in cellular senescence (such as TP53 function and mTOR signaling), and genes involved in the senescence-associated secretory phenotype (such as *IGFBP7*, *IGFBP5*, and *IGFBP4*) were decreased after *SPP1* KD (Table S6). Overall, these findings demonstrate that although elevated *SPP1* levels are not sufficient to establish an inflammatory signature in healthy neurons, in the setting of FTD, expression of *SPP1* is potentially an important driver of a pro-inflammatory signature.

Notably, KD of *SPP1* in FTD neurons also resulted in negative enrichment of genes that were upregulated in cultured FTD iPSC-derived neurons (Figure 7B). Thus, we investigated if *SPP1* KD in FTD neurons would result in altered mitochondrial function, which was disturbed in FTD iPSC neurons (Figure 3). Assays on oxidative stress responses in FTD^{shSPP1} neurons revealed a reversal of vulnerability toward oligomycin, which inhibits the ATP synthase (complex V) in mitochondria (Figure 7C). A similar effect was also noted in Ctrl neurons after KD of *SPP1*, indicating that the beneficial effects of *SPP1* KD on cell survival are not specific to FTD neurons (Figure S5G). *SPP1* KD in FTD neurons did not affect mitophagy (Figure S5H), as similarly seen in FTD and Ctrl neurons with overexpression or downregulation of *MAPT*, respectively (Figures S2T and S2W). However, FTD^{shSPP1} neurons showed reduced levels of OCR (Figure 7D); reduced production of ATP (Figure 7E); and reduced levels of metabolic substrates associated with glycolysis, TCA cycle, and amino acid synthesis (Figure 7F). These findings pointed toward a reduced catabolic state in FTD^{shSPP1} neurons. ^{13}C carbon tracing analyses revealed reduced utilization of ^{13}C-labeled glucose and ^{13}C-labeled glutamine for the synthesis of various amino acids in FTD^{shSPP1} neurons (Figures 7G and S5I). In addition and in contrast to glucose-derived ^{13}C, FTD^{shSPP1} neurons also showed decreased incorporation of glutamine-derived ^{13}C into intermediates of the TCA cycle and thus reduced utilization of amino acids for energy consumption, further highlighting a modulatory role of *SPP1* on oxidative metabolism (Figures 7G and S5I).

We next wondered if *SPP1* KD would lead to increased engraftment of FTD neurons and reduce microglial infiltration *in vivo*. Thus, we injected FTD^{shSPP1} or FTD^{scr} NPCs into the forebrains of NSG mice. Prior to cell injection, we confirmed that *SPP1* KD leads to a significant reduction of secreted OPN protein (Figure 7H). 4 months after transplantation, grafts were identified in both groups and were composed of $hNCAM^+$ cells (Figures 7I–7L). However, FTD^{shSPP1} neuronal grafts showed increased hNCAM positivity and increased outgrowth of $hNCAM^+$ fibers into the surrounding brain parenchyma when compared with FTD^{scr} neuronal grafts, indicating improved engraftment of FTD neurons after *SPP1* KD (Figures 7J–7M). Notably, this finding was paralleled by reduced microglial infiltration, as the number of Iba1^+ microglia adjacent to FTD^{shSPP1} neuronal grafts was significantly reduced compared with FTD^{scr} neuronal grafts (Figures 7N and 7O). Overall, these findings demonstrate that FTD neurons support a microglial response linked OPN/*SPP1* and that KD of OPN/*SPP1* in FTD neurons has a beneficial effect on neuronal engraftment and microglial infiltration in the adult brain.

DISCUSSION

Here, we demonstrate mitochondrial and metabolic pathology in FTD neurons carrying *MAPT-N279K* that is linked to elevated oxygen consumption and increased energy demand with elevated ATP production. These metabolic changes can be targeted since downregulation of oxygen consumption by metformin led to partial reversal of transcriptional dysregulation in cultured neurons. It should be noted, however, that effects on mitochondrial function might depend on the genetic

Please cite this article in press as: Al-Dalahmah et al., Osteopontin drives neuroinflammation and cell loss in *MAPT-N279K* frontotemporal dementia patient neurons, Cell Stem Cell (2024), https://doi.org/10.1016/j.stem.2024.03.013

CellPress
OPEN ACCESS

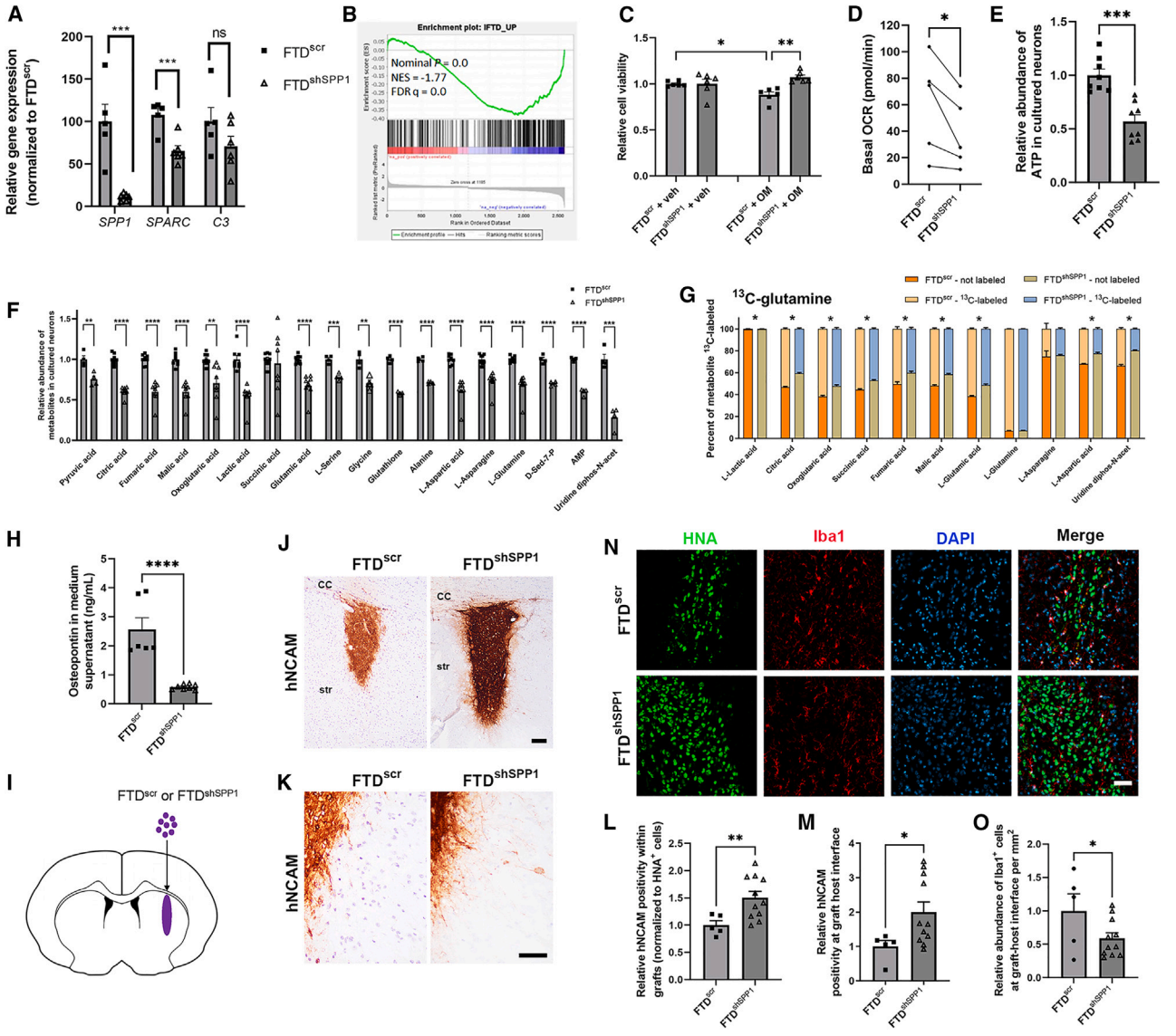

Figure 7. Osteopontin modulates neuronal survival and microglial infiltration around FTD grafts

(A) RT-qPCR for *SPP1*, *SPARC*, and *C3* in FTD neurons after *SPP1* knockdown.

(B) Enrichment plot showing the depletion of genes that are upregulated in cultured FTD-iPSC-derived neurons ("iFTD") in FTD^{shSPP1} neurons. NES, normalized enrichment score.

(C) MTS assay demonstrating the rescue of oligomycin-induced cell death in FTD^{shSPP1} neurons.

(D) Seahorse assay on FTD^{scr} and FTD^{shSPP1} neurons, demonstrating the reduction of basal OCR in FTD^{shSPP1} neurons.

(E) Quantification of ATP in FTD^{scr} and FTD^{shSPP1} neurons.

(F) Quantification of polar metabolites in FTD^{scr} and FTD^{shSPP1} neurons.

(G) Percentages of selected ^{13}C-labeled and ^{12}C-unlabeled metabolites of the TCA cycle and associated pathways after the application of ^{13}C-glutamine to the medium of FTD^{scr} and FTD^{shSPP1} neurons.

(H) ELISA of the medium supernatant of cultured FTD^{scr} and FTD^{shSPP1} neurons for osteopontin.

(I) Schematic drawing of the experimental approach using FTD^{scr} and FTD^{shSPP1} neural cells for transplantation.

(J) Immunohistochemical stainings of FTD^{scr} and FTD^{shSPP1} grafts for hNCAM.

(K) As in (J), but at the graft-host interface.

(L) Quantification of hNCAM positivity within grafts.

(M) Quantification of hNCAM positivity at the graft-host interface.

(N) Immunostainings of FTD^{scr} and FTD^{shSPP1} grafts for Iba-1 and HNA with DAPI counterstaining.

(O) Quantification of Iba-1^{+} microglial cells around FTD^{scr} and FTD^{shSPP1} grafts.

Scale bars: 50 μm (K and N) and 100 μm (J). *$p < 0.05$ and **$p < 0.01$, ***$p < 0.001$, ****$p < 0.0001$—one-tailed Student's t test (A, D–F, H, L, M, and O), multiple t test (G), or one-way ANOVA with Dunnett's multiple comparisons test (C). Data are presented as mean + SEM (+ SD in G). See also Figure S5.

Please cite this article in press as: Al-Dalahmah et al., Osteopontin drives neuroinflammation and cell loss in *MAPT-N279K* frontotemporal dementia patient neurons, Cell Stem Cell (2024), https://doi.org/10.1016/j.stem.2024.03.013

background in FTD since decreased oxidative phosphorylation was observed in iPSC neurons that carry an FTD-associated mutation in the *CHMP2B* gene.[30] Also, lower ATP production by oxidative phosphorylation was found in iPSC neurons carrying the 10 + 16 mutation in *MAPT*.[31] iPSC neurons with *C9orf72* hexanucleotide expansion exhibit reduced oxidative phosphorylation and complex-1 activity,[32] and neurons carrying a *TARDBP-G298S* mutation showed a decreased OCR.[33] Conversely, differentiated FTD iPSC neurons with homozygous *MAPT-V337M* demonstrated an increased basal and maximal respiration with reduced coupling efficiency and respiratory control ratio and with similar ATP-linked respiration.[9] We found increased oxidative phosphorylation in iPSC neurons carrying heterozygous and homozygous *MAPT-P301L*. However, *MAPT-P301L*-mutant neurons did not show decreased mitophagy that we had observed in *MAPT-N279K* neurons (Figure S2G). Published literature and our findings thus suggest that altered mitochondrial function strongly depends on the underlying FTD mutation and that our findings on increased oxidative phosphorylation in FTD neurons are not generalizable to all forms of FTD. A thorough analysis of potentially altered tau interactions with mitochondrial proteins across different sporadic and genetic subtypes of FTD may provide further insights into mitochondrial function in FTD and may explain observed differences in mitochondrial respiration. Such altered tau interactome was recently demonstrated for the *MAPT-P301L* and *MAPT-V337M* mutations in FTD neurons, which resulted in weakened interaction of tau with specific mitochondrial molecules in a mutation-specific manner.[9]

We have observed a pronounced microglial response in postmortem FTD brains, which is in line with previous reports of reactive microglia in areas of neuronal degeneration in sporadic and familial forms of FTD.[11,34] Although several groups have identified FTD-associated polymorphisms or mutations in genes that are directly linked to neuroinflammation,[35] it is still not known how microglia cause neuronal damage. We demonstrate that FTD neurons express elevated levels of pro-inflammatory molecules and carry a robust pro-inflammatory gene signature, as seen in cultured FTD neurons, FTD neuronal grafts, and postmortem brains. Importantly, transplanted FTD neurons elicited an increased microglial response with increased number of microglia carrying a reactive gene signature relevant to FTD as evidenced by snRNA-seq. These observations indicated a potential immune-regulatory function of neurons in FTD by inducing a microglial response.

We identified *SPP1*/OPN as one of the pro-inflammatory molecules in FTD neurons, which altered neuronal viability and microglial response. OPN is an extracellular matrix protein and secreted cytokine mainly expressed in activated macrophages, T lymphocytes, and microglia.[36] While OPN has a neuroprotective function in ischemia and hemorrhagic stroke,[36,37] its expression was associated with a detrimental, pro-inflammatory effect in multiple sclerosis,[38] PD, and Alzheimer's disease (AD).[39–41] Increased levels of OPN were detected in the CSF of PD and AD patients and positively correlated with cognitive impairment in both diseases.[40,42,43] Although OPN levels are significantly elevated in the CSF of patients with FTD,[44] the functional role of OPN in the context of FTD is unknown. We found upregulation of *SPP1*/OPN in FTD neurons, which influenced neuronal function and survival since downregulation of OPN in FTD neurons resulted in reversal of oxidative stress linked to complex V and in downregulation of inflammation-associated genes and pathways. Furthermore, downregulation of OPN caused decreased oxidative phosphorylation, ATP production, and the overall catabolic state in FTD neurons; and it improved the engraftment of FTD neurons after transplantation into the mouse brain. Increased levels of OPN were also detected in SN DA neurons of patients with PD, and in OPN knockout mice, DA neurons demonstrated reduced vulnerability toward MPTP-mediated cell stress paralleled by reduced numbers of microglial cells, pointing toward a disease-accelerating effect of OPN upon neuronal cell stress.[40] An upregulation of OPN was also seen in hippocampal CA1 neurons of AD patients, but its function in these neurons remains unknown.[45]

The effects of OPN on microglial function are complex, context-dependent, and incompletely understood.[36,39,46] For instance, OPN increases survival of rat primary microglia upon LPS-induced stress and shifts the microglial inflammatory profile toward a neutral anti-inflammatory phenotype.[47] At the same time, *SPP1*/OPN is an integral part of the disease-associated microglia (DAM) signature in AD,[48] its expression is upregulated in microglia surrounding amyloid plaques,[49] and it recruits microglia to phagocytose synapses.[50] Like our findings in HMC-3 cells, OPN increases phagocytosis in porcine microglia[51] and in rat brain macrophages in a stroke model,[52] but such a pro-phagocytic effect was not seen in rat primary microglia.[47]

We found that OPN upregulated some of the reactive-associated genes in cultured human microglia, which were also upregulated in microglia in postmortem FTD brains. We also identified significant effects of OPN on microglia *in vivo*, as overexpression of OPN in transplanted Ctrl neural cells resulted in an increased number of graft-associated mouse microglia. Likewise, downregulation of OPN in transplanted FTD neurons led to reduced microglial infiltration. Thus, OPN could represent a potential molecular target to address pathology in FTD, encouraging further study of the mechanisms that lead to OPN-mediated changes in neurons and glial cells in FTD.

Limitations of the study

Several questions remain unanswered and limit the extension of our study's conclusions. First, our postmortem snRNA-seq analyses were performed on one brain region that is prone to neurodegeneration, and our findings may not generalize to other brain regions. Additional areas from the same patients as well as from a larger number of patients with other sporadic and familial forms of FTD and related tauopathies should be examined to generate a more complete single-cell brain atlas for FTD and related dementias. Such an analysis would also indicate if potential molecular targets such as OPN are region-, gender-, age-, FTD subtype-, mutation-, and disease-specific or are even conserved between different forms of FTD and related diseases. Second, we studied the effects of OPN as one potential molecular target in FTD, but it is highly

unlikely that OPN alone drives pathology in FTD but rather a combination of multiple factors that need to be explored. Third, it is possible that a proportion of the pathology in our graft model is explained by NPCs or astrocytes that survive in the graft. However, both populations represented a small minority of the cells in the grafts. Also, a robust pro-inflammatory phenotype was not apparent in engrafted astrocytes, and postmortem astrocytes appear to have a loss-of-function phenotype (Figure S6; Table S7). Still, additional studies are needed to disentangle the effects of astrocytes in the pathology of FTD *in vivo*. Finally, only male mice were used. Future comparisons between female and male mice could identify sex-specific changes in brains with stem cell grafts.

STAR★METHODS

Detailed methods are provided in the online version of this paper and include the following:

- KEY RESOURCES TABLE
- RESOURCE AVAILABILITY
  - Lead contact
  - Materials availability
  - Data and code availability
- EXPERIMENTAL MODELS AND STUDY PARTICIPANT DETAILS
  - Human subjects and brain tissue
  - Culture of human iPSCs
  - Generation of MAPT-P301L knockin hiPSCs
  - Neuronal differentiation of human iPSCs
  - Microglial differentiation of human iPSCs
- METHOD DETAILS
  - Flow cytometry for ROS production
  - Phagocytosis assay
  - Immunocytochemistry
  - Lentiviral transduction of NPCs and neurons
  - Seahorse mito stress assay
  - Mass spectrometry and isotope tracing
  - Transplantation
  - Immunohistochemistry
  - Quantitative analysis of grafts and host glia
  - Microdissection of grafts
  - *In situ* hybridization
  - Quantitative RT-PCR
  - Microarray
  - Bulk RNA sequencing
  - Extraction of nuclei and snRNA-seq procedure
  - Single nucleus RNA-seq analysis
- QUANTIFICATION AND STATISTICAL ANALYSIS

SUPPLEMENTAL INFORMATION

Supplemental information can be found online at https://doi.org/10.1016/j.stem.2024.03.013.

ACKNOWLEDGMENTS

We would like to thank all the patients and their families for the brain donations. We also thank Archana Ashok for technical assistance in sgRNA design, cloning, and validation for *MAPT-P301L* genome editing. Mass spectrometric analyses were performed at the Weill Cornell Medicine Proteomics and Metabolomics Core Facility. Microarray analyses were performed at the Boston University Microarray and Sequencing Resource Core Facility. This work was supported by NIH grants R03NS112785, R21AG070414-01, and K08NS116166-01 to G.H. G.H. was also supported by NIH grants R25NS070697 and P50AG008702. O.A.-D. was supported by the Hereditary Disease Foundation, Huntington Disease Society of America, and the American Brain Tumor Association Discover grant —fully supported by the Uncle Kory Foundation, the NIH/NIA (AG075754), and the NIA/Columbia University ADRC grant P30AG066462. G.H. and A.A.S. were supported by the Henry and Marilyn Taub Foundation, the Thompson Family Foundation (TAME-AD; GT006988-19), and NIA/Columbia University ADRC grant P30AG066462. Z.K.W. is partially supported by the NIH/NIA and NIH/NINDS (1U19AG063911, FAIN: U19AG063911), the Mayo Clinic Center for Regenerative Medicine, gifts from the Donald G. and Jodi P. Heeringa Family, the Haworth Family Professorship in Neurodegenerative Diseases fund, The Albertson Parkinson's Research Foundation, the PPND Family Foundation, and the Margaret N. and John Wilchek Family. The graphical abstract was created with BioRender.com.

AUTHOR CONTRIBUTIONS

O.A.-D., M.L., J.J.M., W.Q., T.N., J.-Y.M., S.K., N.I., T.W., R.K., Y.A.K., M.C.D.R., and G.H. conducted and analyzed experiments. A. Mahajan, N.H., E.A., and H.L. conducted experiments. K.A.J. and F.P. analyzed and processed data. O.A.-D., M.L., V.M., and G.H. analyzed and interpreted snRNA-seq data. M.A.D., X.F., J.P.V., Z.K.W., D.W.D., T.K., H.Z., H.R.S., and A.A.S. provided cell lines or postmortem brain tissue. O.A.-D., M.L., J.J.M., C.A.D., A.D., A. Mela, A.A.S., M.D.S., P.L.D.J., J.E.G., V.M., P.C., and G.H. discussed and interpreted data. O.A.-D., M.L., J.J.M., and G.H. designed experiments and wrote the paper. G.H. led and supervised the study. All authors reviewed and approved the paper.

DECLARATION OF INTERESTS

Z.K.W. serves as PI or co-PI on Biohaven Pharmaceuticals, Inc. (BHV4157-206), Vigil Neuroscience, Inc. (VGL101-01.002, VGL101-01.201), and ONO-2808-03 projects/grants. He serves as co-PI of the Mayo Clinic APDA Center for Advanced Research and as an external advisory board member for Vigil Neuroscience, Inc. and as a consultant for Eli Lilly & Company and for NovoGlia, Inc.

Received: April 4, 2023
Revised: January 7, 2024
Accepted: March 19, 2024
Published: April 15, 2024

REFERENCES

1. Bird, T., Knopman, D., VanSwieten, J., Rosso, S., Feldman, H., Tanabe, H., Graff-Raford, N., Geschwind, D., Verpillat, P., and Hutton, M. (2003). Epidemiology and genetics of frontotemporal dementia/Pick's disease. Ann. Neurol. *54*, S29–S31. https://doi.org/10.1002/ana.10572.
2. Goedert, M., Spillantini, M.G., Jakes, R., Rutherford, D., and Crowther, R.A. (1989). Multiple isoforms of human microtubule-associated protein tau: sequences and localization in neurofibrillary tangles of Alzheimer's disease. Neuron *3*, 519–526. https://doi.org/10.1016/0896-6273(89)90210-9.
3. Goedert, M., and Jakes, R. (1990). Expression of separate isoforms of human tau protein: correlation with the tau pattern in brain and effects on tubulin polymerization. EMBO J. *9*, 4225–4230. https://doi.org/10.1002/j.1460-2075.1990.tb07870.x.
4. Ghetti, B., Oblak, A.L., Boeve, B.F., Johnson, K.A., Dickerson, B.C., and Goedert, M. (2015). Invited review: frontotemporal dementia caused by microtubule-associated protein tau gene (MAPT) mutations: a chameleon for neuropathology and neuroimaging. Neuropathol. Appl. Neurobiol. *41*, 24–46. https://doi.org/10.1111/nan.12213.

5. Goedert, M., Ghetti, B., and Spillantini, M.G. (2012). Frontotemporal dementia: implications for understanding Alzheimer disease. Cold Spring Harb. Perspect. Med. *2*, a006254. https://doi.org/10.1101/cshperspect.a006254.

6. Iqbal, K., Liu, F., and Gong, C.X. (2016). Tau and neurodegenerative disease: the story so far. Nat. Rev. Neurol. *12*, 15–27. https://doi.org/10.1038/nrneurol.2015.225.

7. Combs, B., Mueller, R.L., Morfini, G., Brady, S.T., and Kanaan, N.M. (2019). Tau and axonal transport misregulation in tauopathies. Adv. Exp. Med. Biol. *1184*, 81–95. https://doi.org/10.1007/978-981-32-9358-8_7.

8. Torres, A.K., Rivera, B.I., Polanco, C.M., Jara, C., and Tapia-Rojas, C. (2022). Phosphorylated tau as a toxic agent in synaptic mitochondria: implications in aging and Alzheimer's disease. Neural Regen. Res. *17*, 1645–1651. https://doi.org/10.4103/1673-5374.332125.

9. Tracy, T.E., Madero-Pérez, J., Swaney, D.L., Chang, T.S., Moritz, M., Konrad, C., Ward, M.E., Stevenson, E., Hüttenhain, R., Kauwe, G., et al. (2022). Tau interactome maps synaptic and mitochondrial processes associated with neurodegeneration. Cell *185*, 712–728.e14. https://doi.org/10.1016/j.cell.2021.12.041.

10. Arnold, S.E., Han, L.Y., Clark, C.M., Grossman, M., and Trojanowski, J.Q. (2000). Quantitative neurohistological features of frontotemporal degeneration. Neurobiol. Aging *21*, 913–919. https://doi.org/10.1016/s0197-4580(00)00173-1.

11. Ishizawa, K., and Dickson, D.W. (2001). Microglial activation parallels system degeneration in progressive supranuclear palsy and corticobasal degeneration. J. Neuropathol. Exp. Neurol. *60*, 647–657. https://doi.org/10.1093/jnen/60.6.647.

12. Ikeda, M., Shoji, M., Kawarai, T., Kawarabayashi, T., Matsubara, E., Murakami, T., Sasaki, A., Tomidokoro, Y., Ikarashi, Y., Kuribara, H., et al. (2005). Accumulation of filamentous tau in the cerebral cortex of human tau R406W transgenic mice. Am. J. Pathol. *166*, 521–531. https://doi.org/10.1016/S0002-9440(10)62274-2.

13. Bevan-Jones, W.R., Cope, T.E., Jones, P.S., Kaalund, S.S., Passamonti, L., Allinson, K., Green, O., Hong, Y.T., Fryer, T.D., Arnold, R., et al. (2020). Neuroinflammation and protein aggregation co-localize across the frontotemporal dementia spectrum. Brain *143*, 1010–1026. https://doi.org/10.1093/brain/awaa033.

14. Sjögren, M., Folkesson, S., Blennow, K., and Tarkowski, E. (2004). Increased intrathecal inflammatory activity in frontotemporal dementia: pathophysiological implications. J. Neurol. Neurosurg. Psychiatry *75*, 1107–1111. https://doi.org/10.1136/jnnp.2003.019422.

15. Slowinski, J., Dominik, J., Uitti, R.J., Ahmed, Z., Dickson, D.D., and Wszolek, Z.K. (2007). Frontotemporal dementia and Parkinsonism linked to chromosome 17 with the N279K tau mutation. Neuropathology *27*, 73–80. https://doi.org/10.1111/j.1440-1789.2006.00742.x.

16. Moore, K.M., Nicholas, J., Grossman, M., McMillan, C.T., Irwin, D.J., Massimo, L., Van Deerlin, V.M., Warren, J.D., Fox, N.C., Rossor, M.N., et al. (2020). Age at symptom onset and death and disease duration in genetic frontotemporal dementia: an international retrospective cohort study. Lancet Neurol. *19*, 145–156. https://doi.org/10.1016/S1474-4422(19)30394-1.

17. Boeve, B.F., and Rosen, H. (2021). Clinical and neuroimaging aspects of familial frontotemporal lobar degeneration associated with MAPT and GRN mutations. Adv. Exp. Med. Biol. *1281*, 77–92. https://doi.org/10.1007/978-3-030-51140-1_6.

18. Delisle, M.B., Murrell, J.R., Richardson, R., Trofatter, J.A., Rascol, O., Soulages, X., Mohr, M., Calvas, P., and Ghetti, B. (1999). A mutation at codon 279 (N279K) in exon 10 of the Tau gene causes a tauopathy with dementia and supranuclear palsy. Acta Neuropathol. *98*, 62–77. https://doi.org/10.1007/s004010051052.

19. Wilhelmus, M.M., Bol, J.G., Van Haastert, E.S., Rozemuller, A.J., Bu, G., Drukarch, B., and Hoozemans, J.J. (2011). Apolipoprotein E and LRP1 increase early in Parkinson's disease pathogenesis. Am. J. Pathol. *179*, 2152–2156. https://doi.org/10.1016/j.ajpath.2011.07.021.

20. Ehrlich, M., Hallmann, A.L., Reinhardt, P., Araúzo-Bravo, M.J., Korr, S., Röpke, A., Psathaki, O.E., Ehling, P., Meuth, S.G., Oblak, A.L., et al. (2015). Distinct neurodegenerative changes in an induced pluripotent stem cell model of frontotemporal dementia linked to mutant Tau protein. Stem Cell Rep. *5*, 83–96. https://doi.org/10.1016/j.stemcr.2015.06.001.

21. Hallmann, A.L., Araúzo-Bravo, M.J., Mavrommatis, L., Ehrlich, M., Röpke, A., Brockhaus, J., Missler, M., Sterneckert, J., Schöler, H.R., Kuhlmann, T., et al. (2017). Astrocyte pathology in a human neural stem cell model of frontotemporal dementia caused by mutant Tau protein. Sci. Rep. *7*, 42991. https://doi.org/10.1038/srep42991.

22. Reinhardt, P., Glatza, M., Hemmer, K., Tsytsyura, Y., Thiel, C.S., Höing, S., Moritz, S., Parga, J.A., Wagner, L., Bruder, J.M., et al. (2013). Derivation and expansion using only small molecules of human neural progenitors for neurodegenerative disease modeling. PLoS One *8*, e59252. https://doi.org/10.1371/journal.pone.0059252.

23. Hargus, G., Ehrlich, M., Araúzo-Bravo, M.J., Hemmer, K., Hallmann, A.L., Reinhardt, P., Kim, K.P., Adachi, K., Santourlidis, S., Ghanjati, F., et al. (2014). Origin-dependent neural cell identities in differentiated human iPSCs in vitro and after transplantation into the mouse brain. Cell Rep. *8*, 1697–1703. https://doi.org/10.1016/j.celrep.2014.08.014.

24. Kim, Y.A., Siddiqui, T., Blaze, J., Cosacak, M.I., Winters, T., Kumar, A., Tein, E., Sproul, A.A., Teich, A.F., Bartolini, F., et al. (2023). RNA methyltransferase NSun2 deficiency promotes neurodegeneration through epitranscriptomic regulation of tau phosphorylation. Acta Neuropathol. *145*, 29–48. https://doi.org/10.1007/s00401-022-02511-7.

25. Ramaglia, V., Hughes, T.R., Donev, R.M., Ruseva, M.M., Wu, X., Huitinga, I., Baas, F., Neal, J.W., and Morgan, B.P. (2012). C3-dependent mechanism of microglial priming relevant to multiple sclerosis. Proc. Natl. Acad. Sci. USA *109*, 965–970. https://doi.org/10.1073/pnas.1111924109.

26. Mittal, M., Siddiqui, M.R., Tran, K., Reddy, S.P., and Malik, A.B. (2014). Reactive oxygen species in inflammation and tissue injury. Antioxid. Redox Signal. *20*, 1126–1167. https://doi.org/10.1089/ars.2012.5149.

27. Esteras, N., Kopach, O., Maiolino, M., Lariccia, V., Amoroso, S., Qamar, S., Wray, S., Rusakov, D.A., Jaganjac, M., and Abramov, A.Y. (2022). Mitochondrial ROS control neuronal excitability and cell fate in frontotemporal dementia. Alzheimers Dement. *18*, 318–338. https://doi.org/10.1002/alz.12394.

28. Korn, L., Speicher, A.M., Schroeter, C.B., Gola, L., Kaehne, T., Engler, A., Disse, P., Fernández-Orth, J., Csatári, J., Naumann, M., et al. (2023). MAPT genotype-dependent mitochondrial aberration and ROS production trigger dysfunction and death in cortical neurons of patients with hereditary FTLD. Redox Biol. *59*, 102597. https://doi.org/10.1016/j.redox.2022.102597.

29. McQuade, A., Coburn, M., Tu, C.H., Hasselmann, J., Davtyan, H., and Blurton-Jones, M. (2018). Development and validation of a simplified method to generate human microglia from pluripotent stem cells. Mol. Neurodegener. *13*, 67. https://doi.org/10.1186/s13024-018-0297-x.

30. Zhang, Y., Schmid, B., Nikolaisen, N.K., Rasmussen, M.A., Aldana, B.I., Agger, M., Calloe, K., Stummann, T.C., Larsen, H.M., Nielsen, T.T., et al. (2017). Patient iPSC-derived neurons for disease modeling of frontotemporal dementia with mutation in CHMP2B. Stem Cell Rep. *8*, 648–658. https://doi.org/10.1016/j.stemcr.2017.01.012.

31. Esteras, N., Rohrer, J.D., Hardy, J., Wray, S., and Abramov, A.Y. (2017). Mitochondrial hyperpolarization in iPSC-derived neurons from patients of FTDP-17 with 10+16 MAPT mutation leads to oxidative stress and neurodegeneration. Redox Biol. *12*, 410–422. https://doi.org/10.1016/j.redox.2017.03.008.

32. Wang, T., Liu, H., Itoh, K., Oh, S., Zhao, L., Murata, D., Sesaki, H., Hartung, T., Na, C.H., and Wang, J. (2021). C9orf72 regulates energy homeostasis by stabilizing mitochondrial complex I assembly. Cell Metab. *33*, 531–546.e9. https://doi.org/10.1016/j.cmet.2021.01.005.

33. Hor, J.H., Santosa, M.M., Lim, V.J.W., Ho, B.X., Taylor, A., Khong, Z.J., Ravits, J., Fan, Y., Liou, Y.C., Soh, B.S., and Ng, S.Y. (2021). ALS motor

neurons exhibit hallmark metabolic defects that are rescued by SIRT3 activation. Cell Death Differ. *28*, 1379–1397. https://doi.org/10.1038/s41418-020-00664-0.

34. Lant, S.B., Robinson, A.C., Thompson, J.C., Rollinson, S., Pickering-Brown, S., Snowden, J.S., Davidson, Y.S., Gerhard, A., and Mann, D.M. (2014). Patterns of microglial cell activation in frontotemporal lobar degeneration. Neuropathol. Appl. Neurobiol. *40*, 686–696. https://doi.org/10.1111/nan.12092.

35. Hartnell, I.J., Blum, D., Nicoll, J.A.R., Dorothee, G., and Boche, D. (2021). Glial cells and adaptive immunity in frontotemporal dementia with tau pathology. Brain *144*, 724–745. https://doi.org/10.1093/brain/awaa457.

36. Yu, H., Liu, X., and Zhong, Y. (2017). The effect of osteopontin on microglia. BioMed Res. Int. *2017*, 1879437. https://doi.org/10.1155/2017/1879437.

37. Suzuki, H., Hasegawa, Y., Kanamaru, K., and Zhang, J.H. (2010). Mechanisms of osteopontin-induced stabilization of blood-brain barrier disruption after subarachnoid hemorrhage in rats. Stroke *41*, 1783–1790. https://doi.org/10.1161/STROKEAHA.110.586537.

38. Chabas, D., Baranzini, S.E., Mitchell, D., Bernard, C.C., Rittling, S.R., Denhardt, D.T., Sobel, R.A., Lock, C., Karpuj, M., Pedotti, R., et al. (2001). The influence of the proinflammatory cytokine, osteopontin, on autoimmune demyelinating disease. Science *294*, 1731–1735. https://doi.org/10.1126/science.1062960.

39. Cappellano, G., Vecchio, D., Magistrelli, L., Clemente, N., Raineri, D., Barbero Mazzucca, C., Virgilio, E., Dianzani, U., Chiocchetti, A., and Comi, C. (2021). The Yin-Yang of osteopontin in nervous system diseases: damage versus repair. Neural Regen. Res. *16*, 1131–1137. https://doi.org/10.4103/1673-5374.300328.

40. Maetzler, W., Berg, D., Schalamberidze, N., Melms, A., Schott, K., Mueller, J.C., Liaw, L., Gasser, T., and Nitsch, C. (2007). Osteopontin is elevated in Parkinson's disease and its absence leads to reduced neurodegeneration in the MPTP model. Neurobiol. Dis. *25*, 473–482. https://doi.org/10.1016/j.nbd.2006.10.020.

41. Carecchio, M., and Comi, C. (2011). The role of osteopontin in neurodegenerative diseases. J. Alzheimers Dis. *25*, 179–185. https://doi.org/10.3233/JAD-2011-102151.

42. Sun, Y., Yin, X.S., Guo, H., Han, R.K., He, R.D., and Chi, L.J. (2013). Elevated osteopontin levels in mild cognitive impairment and Alzheimer's disease. Mediators Inflamm. *2013*, 615745. https://doi.org/10.1155/2013/615745.

43. Comi, C., Carecchio, M., Chiocchetti, A., Nicola, S., Galimberti, D., Fenoglio, C., Cappellano, G., Monaco, F., Scarpini, E., and Dianzani, U. (2010). Osteopontin is increased in the cerebrospinal fluid of patients with Alzheimer's disease and its levels correlate with cognitive decline. J. Alzheimers Dis. *19*, 1143–1148. https://doi.org/10.3233/JAD-2010-1309.

44. Mattsson, N., Rüetschi, U., Pijnenburg, Y.A., Blankenstein, M.A., Podust, V.N., Li, S., Fagerberg, I., Rosengren, L., Blennow, K., and Zetterberg, H. (2008). Novel cerebrospinal fluid biomarkers of axonal degeneration in frontotemporal dementia. Mol. Med. Rep. *1*, 757–761. https://doi.org/10.3892/mmr_00000025.

45. Wung, J.K., Perry, G., Kowalski, A., Harris, P.L., Bishop, G.M., Trivedi, M.A., Johnson, S.C., Smith, M.A., Denhardt, D.T., and Atwood, C.S. (2007). Increased expression of the remodeling- and tumorigenic-associated factor osteopontin in pyramidal neurons of the Alzheimer's disease brain. Curr. Alzheimer Res. *4*, 67–72. https://doi.org/10.2174/156720507779939869.

46. Rosmus, D.D., Lange, C., Ludwig, F., Ajami, B., and Wieghofer, P. (2022). The role of osteopontin in microglia biology: current concepts and future perspectives. Biomedicines *10*, 840. https://doi.org/10.3390/biomedicines10040840.

47. Rabenstein, M., Vay, S.U., Flitsch, L.J., Fink, G.R., Schroeter, M., and Rueger, M.A. (2016). Osteopontin directly modulates cytokine expression of primary microglia and increases their survival. J. Neuroimmunol. *299*, 130–138. https://doi.org/10.1016/j.jneuroim.2016.09.009.

48. Keren-Shaul, H., Spinrad, A., Weiner, A., Matcovitch-Natan, O., Dvir-Szternfeld, R., Ulland, T.K., David, E., Baruch, K., Lara-Astaiso, D., and Toth, B. (2017). A unique microglia type associated with restricting development of Alzheimer's disease. Cell *169*, 1276–1290.e17. e1217. https://doi.org/10.1016/j.cell.2017.05.018.

49. Rentsendorj, A., Sheyn, J., Fuchs, D.T., Daley, D., Salumbides, B.C., Schubloom, H.E., Hart, N.J., Li, S., Hayden, E.Y., Teplow, D.B., et al. (2018). A novel role for osteopontin in macrophage-mediated amyloid-beta clearance in Alzheimer's models. Brain Behav. Immun. *67*, 163–180. https://doi.org/10.1016/j.bbi.2017.08.019.

50. De Schepper, S., Ge, J.Z., Crowley, G., Ferreira, L.S.S., Garceau, D., Toomey, C.E., Sokolova, D., Rueda-Carrasco, J., Shin, S.H., Kim, J.S., et al. (2023). Perivascular cells induce microglial phagocytic states and synaptic engulfment via SPP1 in mouse models of Alzheimer's disease. Nat. Neurosci. *26*, 406–415. https://doi.org/10.1038/s41593-023-01257-z.

51. Tambuyzer, B.R., Casteleyn, C., Vergauwen, H., Van Cruchten, S., and Van Ginneken, C. (2012). Osteopontin alters the functional profile of porcine microglia in vitro. Cell Biol. Int. *36*, 1233–1238. https://doi.org/10.1042/CBI20120172.

52. Shin, Y.J., Kim, H.L., Choi, J.S., Choi, J.Y., Cha, J.H., and Lee, M.Y. (2011). Osteopontin: correlation with phagocytosis by brain macrophages in a rat model of stroke. Glia *59*, 413–423. https://doi.org/10.1002/glia.21110.

53. Bankhead, P., Loughrey, M.B., Fernández, J.A., Dombrowski, Y., McArt, D.G., Dunne, P.D., McQuaid, S., Gray, R.T., Murray, L.J., Coleman, H.G., et al. (2017). QuPath: open source software for digital pathology image analysis. Sci. Rep. *7*, 16878. https://doi.org/10.1038/s41598-017-17204-5.

54. Ulgen, E., Ozisik, O., and Sezerman, O.U. (2019). pathfindR: an R package for comprehensive identification of enriched pathways in omics data through active subnetworks. Front. Genet. *10*, 858. https://doi.org/10.3389/fgene.2019.00858.

55. Cao, J., Spielmann, M., Qiu, X., Huang, X., Ibrahim, D.M., Hill, A.J., Zhang, F., Mundlos, S., Christiansen, L., Steemers, F.J., et al. (2019). The single-cell transcriptional landscape of mammalian organogenesis. Nature *566*, 496–502. https://doi.org/10.1038/s41586-019-0969-x.

56. Gautier, L., Cope, L., Bolstad, B.M., and Irizarry, R.A. (2004). affy–analysis of Affymetrix GeneChip data at the probe level. Bioinformatics *20*, 307–315. https://doi.org/10.1093/bioinformatics/btg405.

57. Gentleman, R.C., Carey, V.J., Bates, D.M., Bolstad, B., Dettling, M., Dudoit, S., Ellis, B., Gautier, L., Ge, Y., Gentry, J., et al. (2004). Bioconductor: open software development for computational biology and bioinformatics. Genome Biol. *5*, R80. https://doi.org/10.1186/gb-2004-5-10-r80.

58. Wszolek, Z.K., Pfeiffer, R.F., Bhatt, M.H., Schelper, R.L., Cordes, M., Snow, B.J., Rodnitzky, R.L., Wolters, E.C., Arwert, F., and Calne, D.B. (1992). Rapidly progressive autosomal dominant parkinsonism and dementia with pallido-ponto-nigral degeneration. Ann. Neurol. *32*, 312–320. https://doi.org/10.1002/ana.410320303.

59. Sun, J., Carlson-Stevermer, J., Das, U., Shen, M., Delenclos, M., Snead, A.M., Koo, S.Y., Wang, L., Qiao, D., Loi, J., et al. (2019). CRISPR/Cas9 editing of APP C-terminus attenuates beta-cleavage and promotes alpha-cleavage. Nat. Commun. *10*, 53. https://doi.org/10.1038/s41467-018-07971-8.

60. Montesinos, J., Pera, M., Larrea, D., Guardia-Laguarta, C., Agrawal, R.R., Velasco, K.R., Yun, T.D., Stavrovskaya, I.G., Xu, Y., Koo, S.Y., et al. (2020). The Alzheimer's disease-associated C99 fragment of APP regulates cellular cholesterol trafficking. EMBO J. *39*, e103791. https://doi.org/10.15252/embj.2019103791.

61. Slaymaker, I.M., Gao, L., Zetsche, B., Scott, D.A., Yan, W.X., and Zhang, F. (2016). Rationally engineered Cas9 nucleases with improved specificity. Science *351*, 84–88. https://doi.org/10.1126/science.aad5227.

62. Dai, M., Wang, P., Boyd, A.D., Kostov, G., Athey, B., Jones, E.G., Bunney, W.E., Myers, R.M., Speed, T.P., Akil, H., et al. (2005). Evolving gene/transcript definitions significantly alter the interpretation of GeneChip data. Nucleic Acids Res. *33*, e175. https://doi.org/10.1093/nar/gni179.

63. Ritchie, M.E., Phipson, B., Wu, D., Hu, Y., Law, C.W., Shi, W., and Smyth, G.K. (2015). limma powers differential expression analyses for RNA-sequencing and microarray studies. Nucleic Acids Res. *43*, e47. https://doi.org/10.1093/nar/gkv007.

64. Al-Dalahmah, O., Sosunov, A.A., Shaik, A., Ofori, K., Liu, Y., Vonsattel, J.P., Adorjan, I., Menon, V., and Goldman, J.E. (2020). Single-nucleus RNA-seq identifies Huntington disease astrocyte states. Acta Neuropathol. Commun. *8*, 19. https://doi.org/10.1186/s40478-020-0880-6.

65. Krishnaswami, S.R., Grindberg, R.V., Novotny, M., Venepally, P., Lacar, B., Bhutani, K., Linker, S.B., Pham, S., Erwin, J.A., Miller, J.A., et al. (2016). Using single nuclei for RNA-seq to capture the transcriptome of postmortem neurons. Nat. Protoc. *11*, 499–524. https://doi.org/10.1038/nprot.2016.015.

66. Fleming, S.J., Chaffin, M.D., Arduini, A., Akkad, A.D., Banks, E., Marioni, J.C., Philippakis, A.A., Ellinor, P.T., and Babadi, M. (2023). Unsupervised removal of systematic background noise from droplet-based single-cell experiments using CellBender. Nat. Methods *20*, 1323–1335. https://doi.org/10.1038/s41592-023-01943-7.

Please cite this article in press as: Al-Dalahmah et al., Osteopontin drives neuroinflammation and cell loss in *MAPT-N279K* frontotemporal dementia patient neurons, Cell Stem Cell (2024), https://doi.org/10.1016/j.stem.2024.03.013

STAR★METHODS

KEY RESOURCES TABLE

REAGENT or RESOURCE	SOURCE	IDENTIFIER
Antibodies		
goat anti-Osteopontin	R&D Systems	Cat# AF1433; RRID:AB_354791
rabbit IgG control	R&D Systems	Cat# AB-105-C; RRID:AB_354266
mouse anti-TUJ1 (βIII-tubulin)	Covance	Cat#BL-801201; RRID:AB_2728521
rabbit anti-TH	Pel-Freez Biologicals	Cat#P40101-150; RRID:AB_2617184
rabbit anti-GABA	MilliporeSigma	Cat#A2052;RRID:AB_477652
rabbit anti-Iba1	Wako	Cat# 019-19741; RRID:AB_839504
mouse anti-TOM20	Santa Cruz Biotechnology	Cat# sc-17764; RRID:AB_628381
rabbit anti-LAMP1	ThermoFisher	Cat# PA1-654A; RRID:AB_2134611
mouse anti-AT8	ThermoFisher	Cat# MN1020;RRID:AB_223647
mouse anti-Synaptic vesicle protein-2	Developmental Studies Hybridoma Bank	Cat# SV2;RRID:AB_2315387
rabbit anti-NeuN	Abcam	Cat# ab104225; RRID:AB_10711153
mouse anti-Human nuclei antigen	MilliporeSigma	Cat# MAB1281; RRID:AB_94090
rabbit anti-Synaptophysin	MilliporeSigma	Cat# SAB4502906; RRID:AB_10746692
mouse anti-Glial fibrillary acidic protein (GFAP)	Chemicon	Cat# MAB360; RRID:AB_11212597
mouse anti-Human-specific GFAP (STEM123)	Takara Bio	Cat# Y40420; RRID:AB_2833249
mouse anti-hNCAM (CD56)	Leica Biosystems	Cat# NCL-CD56-504; RRID:AB_563907
mouse anti-CD68	Agilent	Cat# GA60961-2; RRID:AB_2661840
rabbit anti-AT8 (Phospho tau)	Agilent	Cat# A0024; RRID:AB_10013724
rabbit anti-Opalin (TMEM10)	Abcam	Cat#ab121425; RRID:AB_11127935
AlexaFluor 405 goat anti-mouse IgG	Invitrogen	Cat#A48255; RRID:AB_2890536
AlexaFluor 488 goat anti-mouse IgG	Invitrogen	Cat# A-11001; RRID:AB_2534069
AlexFluor 568 goat anti-rabbit IgG	Invitrogen	Cat# A-11036; RRID:AB_10563566
AlexaFluor 594 goat anti-mouse IgG	Invitrogen	Cat# A-11005; RRID:AB_2534073
AlexaFluor 594 goat anti-rabbit IgG	Invitrogen	Cat# A-11012; RRID:AB_2534079
Bacterial and virus strains		
Human SPP1 overexpression lentivirus	VectorBuilder	Cat#LVM(VB211028-1319gek)-C
Human MAPT overexpression lentivirus	VectorBuilder	Cat#LVS(VB900088-1089xyg)-K1
Negative control lentivirus	VectorBuilder	Cat#LVM(VB010000-9298rtf)-C
Scramble shRNA non-targeting control	Sigma	Cat#SHC016V
Human SPP1 shRNA #1	Sigma	NM_000582; Clone ID TRCN0000004875
Human SPP1 shRNA #2	Sigma	NM_000582; Clone ID TRCN0000342616
Human SPP1 shRNA #3	Sigma	NM_000582; Clone ID TRCN0000342561
Human SPP1 shRNA #4	Sigma	NM_000582; Clone ID TRCN0000004878
Human MAPT shRNA	Sigma	NM_005910; Clone ID TRCN0000083975
Biological samples		
Human postmortem brain tissue	Columbia University Brain Bank, New York, New York; Mayo Clinic Brain Bank, Jacksonville, Florida	See Table S1
Chemicals, peptides, and recombinant proteins		
2-Mercaptoethanol	ThermoFisher	Cat#21985023
ROCKi	Selleck Chemicals	Cat#Y-27632
Human FGF-basic (FGF-2)	Peptrotech	Cat#10018B-50UG
SB-431542	Selleck Chemicals	Cat#S1067
Dorsomorphin	Tocris	Cat#3093

(*Continued on next page*)

Continued

REAGENT or RESOURCE	SOURCE	IDENTIFIER
N2 Supplement	ThermoFisher	Cat#17502048
B27 Supplement without vitamin A	ThermoFisher	Cat#2587010
B27 supplement with vitamin A, serum free	ThermoFisher	Cat#17504044
CHIR99021	Axon MedChem	Cat#1386
Purmorphamine	StemCell Technologies	Cat#72202
Human/Murine FGF-8	Peptrotech	Cat#100-25-25UG
Dibutyryl cyclic-AMP	Sigma	Cat#D0260-100mg
Human GDNF	Peprotech	Cat#450-10-10UG
Animal-free human TGF-beta3	Peptrotech	Cat#AF-100-36E-10UG
Human/Murine/Rat BDNF	Peptrotech	Cat#450-02-10uG
Ascorbic Acid	Sigma	Cat#A4544-100G
Recombinant Human IL-1β	ThermoFisher	Cat#RIL1BI
Recombinant Human IL-34 Protein	R&D Systems	Cat#5265-IL-010/CF
Insulin-Transferrin-Selenium	ThermoFisher	Cat#41400045
MEM Non-Essential Amino Acids Solution	ThermoFisher	Cat#11140050
Human NT3	Peptrotech	Cat#450-03-10UG
Recombinant Human M-CSF	Peptrotech	Cat#300-25
Recombinant Human Fractalkine	StemCell Technologies	Cat#78051.1
Human Insulin	Sigma	Cat #I2643
Recombinant Human Osteopontin	Sigma	Cat#SRP3131-50UG
LPS	Sigma	Cat#L5886-10MG
Metformin	Sigma	Cat#317240
Rotenone	Sigma	Cat#557368-1GM
Oligomycin A	Sigma	Cat#75351-5MG
Antimycin A	Sigma	Cat#A8674-25MG
13C-D-glucose	Cambridge Isotope Laboratories, Inc	Cat#CLM-1396
13C-L-glutamine	Cambridge Isotope Laboratories, Inc	Cat#CLM-1822
13C-palmitic acid	Cambridge Isotope Laboratories, Inc	Cat#CLM-409
Paraformaldehyde	Electron Microscopy Sciences	Cat#50-980-495
HPLC-grade methanol	Sigma	Cat#439193
Critical commercial assays		
CellTiter 96(R) AQueous One Solution Assay	Promega	Cat#G3580
First strand cDNA synthesis kit	Origene	Cat#NP100042
CellRox DeepRed	ThermoFisher	Cat#C10422
Fluorescent latex beads (latex beads-rabbit IgG-FITCcomplex)	Cayman chemical	Cat#400291
Seahorse XFp Extracellular Flux Analyzers	Agilent	Cat#102340-001
RNAscope™ multiplex fluorescent v2	ACDbio	Cat#323110
Predesigned ACDbio™ RNAscope probe- synaptophysin	ACDbio	Cat#311421
Predesigned ACDbio™ RNAscope probes for SPP1	ACDbio	Cat#889751
Predesigned ACDbio™ RNAscope probes for C3	ACDbio	Cat#425111
RNAscope® Probe- Hs-SPARC	ACDbio	Cat#425111
GeneChip™ Human Gene 2.0 ST microarray	ThermoFisher	Cat#902113
Chromium Controller (10x Genomics)	10X Genomics	Cat #120223
Chromium Single Cell 3' Library & Gel Bead Kit v2	10X Genomics	Cat#120237

(*Continued on next page*)

Please cite this article in press as: Al-Dalahmah et al., Osteopontin drives neuroinflammation and cell loss in *MAPT-N279K* frontotemporal dementia patient neurons, Cell Stem Cell (2024), https://doi.org/10.1016/j.stem.2024.03.013

Continued

REAGENT or RESOURCE	SOURCE	IDENTIFIER
Chromium Single Cell A Chip Kit, 48 runs	10X Genomics	Cat#120236
GeneArt genomic cleavage kit	ThermoFisher	Cat#A24372
STEMdiff Hematopoietic Kit	STEMCELL Technologies	Cat#05310
Deposited data		
Microarray data	This study	GEO: GSE230447
Bulk RNA-sequencing data	This study	GEO: GSE230450
snRNA-sequencing data	This study	GEO: GSE230519
Experimental models: Cell lines		
Human iPSC line: Ctrl-1 (F; APOE3/3)	Ehrlich et al.[20]	Ctrl-1
Human iPSC line: Ctrl-2 (F; APOE3/4)	Ehrlich et al.[20]	Ctrl-2
Human iPSC line: Ctrl-3 (iPS (IMR90)-4; F; APOE3/3)	WiCell	WISCi004-B
Human iPSC line: Ctrl-4 (NCRM-5; M; APOE3/4)	RUCDR/Infinity BiologiX	CRMi001-A (RRID:CVCL_1E75)
Human iPSC line: Ctrl-5 (FTD-5-GC; M; APOE3/4)	NINDS Human Cell And Data Repository / Sampled	NH50337
Human iPSC line: Ctrl-6 (FA0000010; M; APOE3/3)	RUCDR/Infinity BiologiX	CUIMCi001-A (RRID:CVCL_EZ99)
Human iPSC-derived NPCs: FTD-1-GC (GC,M; APOE3/3)	Hallmann et al.[21]	FTD-1-GC
Human iPSC-derived NPCs: FTD-2-GC (GC, M; APOE3/3)	Hallmann et al.[21]	FTD-2-GC
Human iPSC line: FTD-1 (M; MAPT-N279K; APOE3/3)	Ehrlich et al.[20]	FTD-1
Human iPSC line: FTD-2 (M; MAPT-N279K; APOE3/3)	Ehrlich et al.[20]	FTD-2
Human iPSC line: FTD-3 (F; MAPT-V337M; APOE3/3)	Ehrlich et al.[20]	FTD-3
Human iPSC line: FTD-4 (M; MAPT-N279K; APOE3/4)	NINDS Human Cell And Data Repository / Sampled	NH50118
Human iPSC line: FTD-5 (M; MAPT-N279K; APOE3/4)	NINDS Human Cell And Data Repository / Sampled	NH50116
Human iPSC line: FTD-6 (F; MAPT-N279K; APOE3/4)	NINDS Human Cell And Data Repository / Sampled	NH50210
Human iPSC line: Ctrl-4$^{P301L/wt}$ (isogenic to NCRM-5; M; MAPT-P301L; APOE3/4)	This study	Ctrl-4$^{P301L/wt}$
Human iPSC line: Ctrl-4$^{P301L/P301L}$(isogenic to NCRM-5; M; MAPT-P301L; APOE3/4)	This study	Ctrl-4$^{P301L/P301L}$
Experimental models: Organisms/strains		
NSG mice	The Jackson Laboratory	NOD.Cg-Prkdc scid Il2rg tm1Wjl/SzJ mice; RRID:IMSR_JAX:005557
Oligonucleotides		
PCR primers	ThermoFisher	See Table S8
Recombinant DNA		
MAPT Exon 10 sgRNA	Addgene	Cat#43860; http://n2t.net/addgene:43860; RRID:Addgene_43860
eSpCas9(1.1)	Addgene	Cat#71814; http://n2t.net/addgene:71814; RRID:Addgene_71814
Software and algorithms		
FCS express 7	De Novo Software	https://denovosoftware.com/
Qupath version0.2	Bankhead et al.[53]	https://qupath.github.io/

(*Continued on next page*)

Continued

REAGENT or RESOURCE	SOURCE	IDENTIFIER
Cavalieri estimator probe	mbf Biosciences	https://www.mbfbioscience.com/products/stereo-investigator
Graphpad Prism 10	GraphPad	https://www.graphpad.com/
Bioconductor software suite (version 2.11)	Bioconductor	https://bioconductor.org/
affyPLM package (version 1.34.0)	Bioconductor	https://www.bioconductor.org/packages/release/bioc/html/affyPLM.html
limma package	Bioconductor	https://bioconductor.org/packages/release/bioc/html/limma.html
R (version 3.5.1)	The R Foundation	https://www.r-project.org/
bcl2fastq2 (version 2.19)	Illumina	https://support.illumina.com/downloads/bcl2fastq-conversion-software-v2-20.html
kallisto (version 0.44.0)	Anaconda	https://anaconda.org/bioconda/kallisto/files?version=0.44.0
Sleuth	Pachter lab	https://pachterlab.github.io/sleuth/
DESeq2	Bioconductor	https://bioconductor.org/packages/release/bioc/html/DESeq2.html
scater	Bioconductor	https://bioconductor.org/packages/release/bioc/html/scater.html
Cellbender	Broad Institute	https://github.com/broadinstitute/CellBender
Seurat version 4.0.3	Satija lab	https://github.com/satijalab/seurat
EdgeR	Bioconductor	https://bioconductor.org/packages/release/bioc/html/edgeR.html
pathfindR	Ulgen et al.[54]	https://github.com/egeulgen/pathfindR
Monocle 3	Cao et al.[55]	https://cole-trapnell-lab.github.io/monocle3/
affy (version 1.36.1)	Gautier et al[56]	https://bioconductor.org/packages/release/bioc/html/affy.html
Bioconductor software suite (version 2.11)	Gentleman et al.[57]	https://bioconductor.org/
Other		
RNeasy Micro Kit	Qiagen	Cat#74004
QIAshredder columns	Qiagen	Cat#79654
Matrigel, growth factor reduced, high concentration	BD Biosciences	Cat#354263
DMEM/F12 media	ThermoFisher	Cat#11320033
Neurobasal Media	ThermoFisher	Cat#10888-022
Collagenase IV	ThermoFisher	Cat#17104019
Accutase	ThermoFisher	Cat#A11105-01
Cultrex	Biotechne	Cat#3434-005-02
ReLeSR	Stem Cell Technologies	Cat#05872
Knockout DMEM	ThermoFisher	Cat#10829018
Knockout Serum Replacement	ThermoFisher	Cat#10828010
Glutamax	ThermoFisher	Cat#35050061
Penicillin/streptomycin/glutamine	ThermoFisher	Cat#10378016
Normal goat serum	Vector Labs	Cat#S-1000
Vectashield mounting medium	Vector Labs	Cat#H1500
Reconstitution buffer	Biotechne	Cat#RB04
DAPI	ThermoFisher	Cat#62248
RNeasy Plus Mini kit	Qiagen	Cat#74134
PowerUp SYBR Green Master Mix for qPCR	ThermoFisher	Cat#A25741
Normal goat serum	Thermofisher	Cat#01-6201
Triton X 100	Sigma	Cat#X100
StemFlex™ Medium Kit	ThermoFisher	Cat#A3349401

Please cite this article in press as: Al-Dalahmah et al., Osteopontin drives neuroinflammation and cell loss in *MAPT-N279K* frontotemporal dementia patient neurons, Cell Stem Cell (2024), https://doi.org/10.1016/j.stem.2024.03.013

RESOURCE AVAILABILITY

Lead contact

Further information and requests for resources and reagents should be directed to and will be fulfilled by the lead contact, Gunnar Hargus (gh2374@cumc.columbia.edu).

Materials availability

This study did not generate new unique reagents.

Data and code availability

- Single nucleus and bulk RNA-seq data as well as microarray data have been deposited at GEO and are publicly available as of the date of publication. Accession numbers are listed in the key resources table.
- This paper does not report original code.
- Any additional information required to reanalyze the data reported in this paper is available from the lead contact upon request.

EXPERIMENTAL MODELS AND STUDY PARTICIPANT DETAILS

Human subjects and brain tissue

Autopsy brain tissue samples were acquired from the Brain Bank at the Mayo Clinic in Jacksonville, Florida, USA, and from the New York Brain Bank at Columbia University, New York, USA. All specimens were obtained by consent at autopsy, have been deidentified and are IRB exempt to protect the identity of each individual. Healthy control individuals did not show signs of cognitive decline or dementia and their brains were devoid of neurodegenerative pathologies. All FTD patients were members of an extended family with a clinical diagnosis of FTD with Parkinsonism[58] and their brains showed abundant p-tau deposition throughout the brain. The *MAPT-N279K* mutation was confirmed by DNA sequencing in all patients. Neuropathologic diagnoses were rendered by specialized neuropathologists. The substantia nigra was dissected from frozen tissue blocks by a board-certified neuropathologist on dry ice. The demographics of the tissue donors are provided in Table S1.

Culture of human iPSCs

The derivation and characterization of induced pluripotent stem cells (iPSCs) from dermal fibroblasts of control donors and individuals carrying the FTD-associated *MAPT-N279K* or *MAPT-V337M* mutations as well as the generation of isogenic cells was described previously by us.[20,21] Additional FTD iPSC lines with the *MAPT-N279K* mutation as well as additional Ctrl iPSC lines were purchased from the NINDS Human Cell and Data Repository. The generation of heterozygous and homozygous *MAPT-P301L* iPSC lines is described below. All iPSC lines are listed in the key resources table. Prior to neuronal differentiation, iPSC colonies were maintained on a layer of mitotically inactivated mouse embryonic fibroblasts (MEFs) in hESC medium consisting of Knockout DMEM (ThermoFisher) with 20% Knockout Serum Replacement (ThermoFisher), 1% nonessential amino acids (NEAA, ThermoFisher), 1 mM beta-mercaptoethanol (ThermoFisher), 1% penicillin/streptomycin/glutamine (ThermoFisher), freshly supplemented with 5 ng/ml FGF2 (Peprotech). iPSCs cells were split at a ratio of 1:6 to 1:8 every 7 days by mechanical disaggregation with 1 mg/ml collagenase IV (ThermoFisher).

Generation of MAPT-P301L knockin hiPSCs

The *MAPT-P301L* mutation was knocked into 1 and 2 alleles of the NCRM5 hiPSC line (RUCDR/Infinity BiologiX) in a similar manner as to what has been done previously for the *APP* V717I (London) mutation.[59,60] In brief, 3 independent sgRNAs targeting exon 10 of *MAPT* were designed using Deskgen.com, cloned into MLM3636, a gift from Keith Joung (Addgene plasmid # 43860; http://n2t.net/addgene:43860; RRID:Addgene_43860) and tested for efficacy in HEK293 (ATCC) using a genomic cleavage kit (GeneArt,ThermoFisher, cat. #A24372). The best sgRNA, sgDG54 was used for editing, and had the sequence: ACGGCGC ATGGGACGTGTGA. The following primers were used to amplify exon 10 of MAPT: S4F: GCTGGAAATCACTCACACTTCT; S4R: TCCGTCATCTGCCCTATTCT. An HDR template was designed encoding the P301L mutation as well as an additional non-coding (intronic) change within the PAM sequence for sgDG54 which also introduced a Sca1 restriction site. Introduced changes are shown below in bolded underline in the HDR sequence. All oligos for genome editing were ordered from Integrated DNA technologies. HDR Mut sequence:

GAAGCTGGATCTTAGCAACGTCCAGTCCAAGTGTGGCTCAAAGGATAATATCAAACACGTCC**T**GGGAGGC GGCAGTGTGAGTAC**T**TTCACACGTCCCATGCGCCGTGCTGTGGCTTGAATTATTA

NCRM5 hiPSC were electoporated (Lonza) with eSpCas9(1.1), a gift from Feng Zhang[61] (Addgene plasmid # 71814; http://n2t.net/addgene:71814; RRID:Addgene_71814), sgDG54, and mutant HDR template, and plated on MEFs with ROCKi (Y-27632; Selleck Chemicals). Resultant colonies were screened by Sca1 cleavage to determine heterozygous versus homozygous knock-in, which was confirmed by Sanger sequencing. The heterozygous (cl.8) and homozygous (cl.61) knock-in clones used in this study were confirmed to have a normal karyotype (Cell Line Genetics).

Neuronal differentiation of human iPSCs

Neural progenitor cells (NPCs) were generated and cultured as previously described.[22–24] Briefly, iPSC colonies were detached from MEFs 3–4 days after splitting using 2 mg/ml collagenase IV. Pieces of colonies were collected by sedimentation and resuspended in human ESC media (without FGF2) supplemented with 10 μM SB-431542 (Selleck Chemicals), 1 μM dorsomorphin (Tocris), 3 μM CHIR 99021 (Axon Medchem), and 0.5 μM purmorphamine (PMA; StemCell Technologies) and subsequently cultured as embryoid bodies (EBs) in Petri dishes. On day 2, media was changed to N2B27 media containing the same small-molecule supplements. N2B27 medium consisted of Dulbecco's modified Eagle's media (DMEM)-F12 (ThermoFisher)/Neurobasal (ThermoFisher) 50:50 with 1:200 N2 supplement (ThermoFisher), 1:100 B27 supplement lacking vitamin A (ThermoFisher), and with 1% penicillin/streptomycin/glutamine (ThermoFisher). On day 4, SB-431542 and dorsomorphin were withdrawn and 150 mM ascorbic acid (AA; Sigma) was added to the media. On day 6, EBs were triturated into smaller pieces and plated on Matrigel-coated (Matrigel, growth factor reduced, high concentration; BD Biosciences) 12-well plates (Corning) in NPC expansion media (N2B27 with CHIR, PMA, and AA). Media was changed every other day and cells were typically split 1:10–1:15 every 5–6 days. For splitting, cells were digested to single cells for approximately 10 min at 37°C using prewarmed Accutase (ThermoFisher). Cells were diluted in DMEM (ThermoFisher) and spun down at 1,000 rpm for 5 min. The cell pellet was resuspended in fresh NPC expansion media and plated on Matrigel-coated cell culture dishes.

For neuronal differentiation of NPCs, expansion media was changed 2 days after splitting to neuronal induction media consisting of N2B27 medium supplemented with 1 μM PMA, 200 μM AA and 10 ng/ml FGF-8 (Peprotech). After 8 days, the neuronal induction media was replaced by neuronal maturation media consisting of N2B27 with 20 ng/ml BDNF, 10 ng/ml GDNF, 1 ng/ml TGF-β3 (Peprotech), 200 μM AA, and 500 μM dbcAMP (Sigma Aldrich). Media was changed every other day and cultures were analyzed after three weeks in maturation conditions.

Microglial differentiation of human iPSCs

Three human Ctrl iPSC lines (Ctrl-4, Ctrl-5 and Ctrl-6) and three human FTD iPSC lines with the *MAPT-N279K* mutation (FTD-4, FTD-5, FTD-6) were maintained in Stemflex (ThermoFisher) on Cultrex (Biotechne). hiPSCs were differentiated into microglia (iMGLs) via bankable hematopoietic progenitors (HPCs), as described previously.[29] In brief, hiPSCs were split using ReLeSR (Stem Cell Technologies) at multiple low densities, and the next day appropriate density of small colonies were differentiated using the STEMdiff hematopoietic kit (Stem Cell Technologies) as directed, with the addition of a full media change at day 7 to clear dead cells. HPCs were harvested on days 12, 14, and 16 of differentiation, and banked in 10%DMSO/45% Media B (SCT kit)/45% KSR (ThermoFisher). HPCs were thawed as needed and plated at a density of 200,000 HPCs/12 well-well. Differentiated microglia were split at days 11-13 post HPC plating by re-plating non-adherent cells 1:1 in 12 well-wells. Microglia were considered terminally differentiated at day 28 post HPC plating, and treated with either vehicle (water), OPN (1 μg/mL; Sigma) or LPS (5 μg/mL; Sigma) for 24 hours before being harvested for RNA isolation.

METHOD DETAILS

Flow cytometry for ROS production

Cells were stained with CellRox Deep Red reagent according to the manufacturer's protocol and were resuspended in 100 μl into 5 mL 12 x 75 mm round bottom tubes for flow cytometric analysis. Cells were analyzed on either the Agilent NovoCyte Penteon (2010284AA, Agilent Technologies, Santa Clara, CA) or NovoCyte Quanteon (2010097, Agilent Technologies, Santa Clara, CA). Data was collected in photodetectors (parameters) with the following optical filters: 488 nm illumination, 488/10 (FSC, Penteon) or 561 nm illumination, 561/14 bandpass (FSC, Quanteon); 488 nm illumination, 488/10 (SSC, Penteon) or 561 nm illumination, 561/14 bandpass (SSC, Quanteon); 405 nm illumination, 445/45 bandpass (DAPI); and 637 nm excitation, 660/20 bandpass (CellRox Deep Red). All lasers output powers of 100 mW. For each sample, approximately 25,000 live cells were recorded based on the gating strategy described below. Samples were acquired at flow rates between 0.5 and 1 μl per second. Flow cytometry data was analyzed as follows: First, cells were roughly gated using a bivariate plot of FSC versus SSC. Doublets were then excluded using a bivariate plot of FSC pulse area versus FCS pulse height. Live cells were selected based on a plot of DAPI versus FSC. Live cells were then assessed for CellRox Deep Red signal using a univariate histogram further portioned based on CellRox Deep Red expression. CellRox Deep Red^{high} were gated for median fluorescence intensity measurements to calculate differences in ROS between groups. Pulse area was used to measure signal in all parameters except for the purpose of excluding doublets. Flow cytometry and cell sorting experiments were performed in the Columbia Stem Cell Initiative Flow Cytometry core facility at Columbia University Irving Medical Center under the leadership of Michael Kissner.

Phagocytosis assay

HMC3 cells were obtained from ATCC. HMC3 cells were seeded in 24 well plates at 5X10^4 cells each well in 0.5ml culture medium (DMEM with 10% FBS medium) and cultured overnight. Next, the cells were cultured in control-neuron conditioned media, FTD-neuron conditioned media containing rabbit IgG control (R&D Systems), or FTD-neuron conditioned media containing anti-OPN IgG (R&D system) at a concentration of 6 μg/mL for 24 hours. Next, we changed the media, added fresh media containing fluorescent latex beads (1:500, latex beads-rabbit IgG-FITC complex - Cayman chemical), and cultured the cells for 30 min at 37°C. Next, the

Please cite this article in press as: Al-Dalahmah et al., Osteopontin drives neuroinflammation and cell loss in *MAPT-N279K* frontotemporal dementia patient neurons, Cell Stem Cell (2024), https://doi.org/10.1016/j.stem.2024.03.013

cells were washed, trypsinized, and analyzed by flowcytometry using a BD Bioscience LSRII flowcytometer. The percentage of $FITC^+$ cells was evaluated by FCS express 7 (De Novo Software) after gating on the live singlet cells.

Immunocytochemistry

Cells were cultured on Matrigel-coated glass coverslips. Cultures were fixed for 20 minutes at 4°C with 4% paraformaldehyde (Electron Microscopy Sciences) in PBS (ThermoFisher) and washed twice with PBS. Permeabilization and blocking was performed in one step using 0.2% Triton X-100 (Sigma Aldrich), 10% normal goat serum (NGS), in PBS for 45 minutes. Coverslips were washed once with PBS and the following primary antibodies were applied overnight at 4°C in 10% NGS in PBS: TUJ1 (βIII-tubulin; 1:1000; Covance), TH (1:500; Pel-Freez Biologicals), GABA (1:5000; MilliporeSigma), Iba1 (1:500; Wako), TOM20 (1:100; Santa Cruz Biotechnology), LAMP1 (1:200; ThermoFisher Scientific), AT8 (p-tau; 1:150; ThermoFisher Scientific), and synaptic vesicle protein-2 (SV-2; 1:100; Developmental Studies Hybridoma Bank). The next day, following three washing steps with PBS, secondary antibodies were applied for one hour at room temperature in in PBS. All secondary antibodies were obtained from ThermoFisher and were conjugated to AlexaFluor fluorochromes. Finally, cells were washed three times with PBS, including a DAPI counterstaining for nuclei in the second washing step. Cells were mounted in Vectashield mounting medium (Vector Labs) and imaged on a Zeiss LSM800 confocal microscope. For quantitative analysis of immunostainings for TUJ1, TH, GABA or AT8, cells in randomly selected visual fields from at least three independent differentiation experiments were counted in a blinded manner.

Lentiviral transduction of NPCs and neurons

Lentivirus expressing human *SPP1* or human *MAPT* was obtained from VectorBuilder. Scrambled RNA lentiviral particles and shRNA lentiviral particles for the downregulation of *SPP1* or *MAPT* were purchased from Sigma. An MOI of 5 was applied for transduction of 50,000 NPCs or neurons, respectively. Details of the virus strains are listed in the key resources table.

Seahorse mito stress assay

Oxygen consumption rate (OCR) was evaluated using the 24-well Seahorse XFp Extracellular Flux Analyzers (Agilent Inc.) according to the manufacturer instructions. Briefly, neuronal cultures were grown to 80-90% density and cells were placed in a CO_2-free incubator for 1 hour. Cells were then exposed to extracellular flux analysis on the Seahorse XFp instrument to perform a mitochondrial stress assay and assess the different OCRs. The following compounds were applied in a sequential order: 2.5 μM oligomycin, 2 μM FCCP, and 0.5 μM rotenone/antimycin. Results were automatically generated in the Seahorse XF Mito Stress Test Report.

Mass spectrometry and isotope tracing

iPSC-derived neurons were grown in neuronal maturation media to 80-90% confluency and cultures were washed with PBS. Polar metabolites were extracted using 80% ice-cold HPLC grade methanol. The supernatant was processed for analysis by mass spectroscopy. For *in vitro* stable isotope tracing experiments, cultures of iPSC neurons were washed with PBS and cells were incubated in neuronal maturation media without glucose, glutamine and phenol red in the presence of either 10mM solution of ^{13}C-D-glucose, 10mM solution of ^{13}C-L-glutamine or 10mM solution of ^{13}C-palmitic acid (Cambridge Isotope Laboratories, Inc; CLM-1396, CLM-1822 and CLM-409, respectively). 24 hours later, polar metabolites were extracted using 80% ice-cold HPLC grade methanol and samples were processed for analysis by mass spectroscopy.

Transplantation

All animal transplantation studies were performed according to protocol AC-AABM1557 examined and approved by the Animal Care and Use Committee of Columbia University. Transplantations were performed as described previously.[23] In brief, iPSC-derived NPCs were treated with Accutase and were resuspended as single cells in PBS (ThermoFisher) at a density of 50,000 cells per μl. Three microliters of the cell suspension were stereotactically injected into the right hemisphere of adult 8 week-old male NSG mice (NOD.Cg-Prkdc scid Il2rg tm1Wjl/SzJ mice; The Jackson Laboratory) by using a Hamilton 7005KH 5 μl syringe and the following stereotactic coordinates for the injection into the right striatum in relation to bregma: anteroposterior: 0.5 mm, mediolateral: +2.0 mm, dorsoventral: -3.5 mm below skull.

Immunohistochemistry

For immunohistochemistry on mouse brain sections, mice were perfused with 4% paraformaldehyde, pH 7.3. Perfused brain tissue was soaked in 15% sucrose overnight, frozen in liquid nitrogen-cooled 2-methyl-butane (MilliporeSigma) and cut on a cryostat at 10 μm. Primary antibodies, used at 4°C overnight, were antibodies to NeuN (1:500; Abcam), human nuclei antigen (HNA; 1:200; Sigma), SV-2 (1:100; Developmental Studies Hybridoma Bank), synaptophysin (1:100; MilliporeSigma), glial fibrillary acidic protein (GFAP; 1:500; Chemicon), human-specific GFAP (STEM123; 1:1000; Takara Bio), and Iba-1 (1:500; Wako). Secondary antibodies conjugated to AlexaFluor (Invitrogen) were applied for one hour at room temperature. Sections were DAPI counterstained and sections were mounted in Vectashield mounting medium (Vector Labs) and imaged on a Leica Thunder microscope and a Zeiss LSM800 confocal microscope.

For immunohistochemistry of human brain sections, formalin fixed and paraffin-embedded human brain sections (7 μm thick) were processed with automated slide-staining instruments (Roche/Ventana and Leica Biosystems) according to the manufacturers' instructions to detect hNCAM (CD56; ready to use, Leica Biosciences), CD68 (ready to use, Agilent) and p-tau (AT8; Agilent). For

visualization, 3,3′-Diaminobenzidine (DAB; hNCAM and AT8) or the alkaline phosphatase (AP; CD68) based staining methods were used. Automated staining for hNCAM was also applied to 10 μm thick mouse brain sections with human grafts. Images were captured using an Olympus BX53 microscope with an Olympus camera DP-72 (Olympus Lifescience).

Quantitative analysis of grafts and host glia

Unbiased estimates of the volume of transplants were calculated using the Cavalieri estimator probe on H&E-stained serial 10 μm-thick brain sections. Cell counts were obtained applying the fractionator probe. Every tenth 10-μm-thick section of the graft was analyzed for the quantification of cells positive for HNA, NeuN or Iba-1. Confocal analysis using an Zeiss LSM 710 confocal microscope as well as a Leica Thunder microscope was performed to assess (co)localization of marker molecules in engrafted cells and mouse cells. To evaluate the percentage of marker coexpressing cells within the grafts, random sampling in graft core and graft periphery was performed at 40x magnification. The quantification of Iba-1^{+} microglia and the quantification of GFAP or hNCAM positivity was performed within the graft and within a 50 μm perimeter around the graft using QuPath software.

Microdissection of grafts

Brains of decapitated mice were placed in a petri dish with ice-cold HBSS and were sliced using a tissue chopper (McIlwain) at a thickness of 400μm. Petri dishes with brain sections in HBSS were placed under a microdissection microscope (Morrell) to microdissect readily visible human grafts using disposable 21 gauge injection needles (BD™). Isolated grafts were placed in PBS and were frozen at -80°C for snRNA-seq.

In situ hybridization

In situ hybridization was done using RNAscope™ multiplex fluorescent v2 (ACDbio) per the manufacturer's protocol in 7-micron paraffin-embedded, formalin-fixed tissue sections. We used predesigned ACDbio™ RNAscope probes for Synaptophysin (Cat# 311421), SPP1 (cat#889751), C3 (cat#430701), and SPARC (cat#425111). Fluorescent IHC images were taken on a Zeiss 810 Axio confocal microscope at 20x or 40X. Brightfield fluorescent images were taken on an Aperio LSM™ slide scanner at 20X and 40X. For quantification of scanned slides (20X magnification), the substantia nigra in the scanned slides of the midbrain sections was annotated by a neuropathologist. We used the positive cell detection function in Qupath v0.2[53] to identify DAPI positive cells, and quantified signal contained in DAPI-positive nuclei only, and not in the cytoplasm. Synaptophysin positive cells were identified by at least three spots in the nucleus, other probes were quantified in Synaptophysin positive cells by at least 2 spots in the nucleus.

Quantitative RT-PCR

Total RNA was isolated from cells using RNeasy columns (QIAGEN) according to the manufacturer's instructions, including a step to remove genomic DNA. RNA concentration and purity were assessed by measuring the optical density at 260 and 280 nm with a Nanodrop Spectrophotometer (ThermoFisher). cDNA synthesis was performed using the First Strand cDNA Synthesis Kit (Origene) following the manufacturer's instructions. Quantitative real-time PCR (QPCR) was performed using *PowerUp* SYBR Green PCR Master Mix (Applied Biosystems) and a Quantstudio 3 real-time PCR machine. The melting curve of each sample was determined to ensure the specificity of the products. Cycling conditions were 40 cycles of 10 seconds 95°C / 30 seconds 60°C / 30 seconds 72°C. The primer sequences are listed in Table S8. The amount of mRNA expression was quantified and normalized to 18s mRNA using the comparative CT method.

Microarray

RNA from microdissected human nigral tissue or iPSC-derived neurons was extracted using RNeasy columns (QIAGEN). Gene expression profiling was performed using a GeneChip™ Human Gene 2.0 ST microarray (ThermoFisher Scientific). Human Gene 2.0 ST CEL files were normalized to produce gene-level expression values using the implementation of the Robust Multiarray Average (RMA) in the *affy* package (version 1.36.1)[56] included in the Bioconductor software suite (version 2.11)[57] and an Entrez Gene-specific probeset mapping (17.0.0) from the Molecular and Behavioral Neuroscience Institute (Brainarray) at the University of Michigan.[62] Array quality was assessed by computing Relative Log Expression (RLE) and Normalized Unscaled Standard Error (NUSE) using the *affyPLM* package (version 1.34.0). Differential gene expression analysis was done using limma package[63] as follows: 1) The design matrix was setup to compare wildtype and mutant cells, FTD or Ctrl subjects. 2) a linear model was fit by calling fit=lmFit(counts, design=design). 3) An empirical Bayes smoothing was applied to the standard errors by calling fit = eBayes(fit). 4) Finally, significant differentially expressed genes were identified by calling topTable(fit, coef=2, number=20000, p.value = 0.05, sort.by = "logFC").

Bulk RNA sequencing

Poly-A pull-down was applied to enrich for mRNAs from total RNA samples followed by library construction using Illumina TruSeq chemistry. Libraries were sequenced at the Columbia Genome Center using Illumina NovaSeq 6000. Samples were multiplexed in each lane yielding targeted number of paired-end 100bp reads for each sample. RTA (Illumina) was used for base calling and bcl2fastq2 (version 2.19) for converting BCL to the fastq format, coupled with adaptor trimming. A pseudoalignment to a kallisto index

Please cite this article in press as: Al-Dalahmah et al., Osteopontin drives neuroinflammation and cell loss in *MAPT-N279K* frontotemporal dementia patient neurons, Cell Stem Cell (2024), https://doi.org/10.1016/j.stem.2024.03.013

created from transcriptomes (Ensembl v96, Human:GRCh38.p12; Mouse:GRCm38.p6) using kallisto (0.44.0) was performed. Differentially expressed genes were identified using Sleuth or DESeq2, R packages designed to test differential expression between experimental groups from RNA-seq counts data.

Extraction of nuclei and snRNA-seq procedure

Nuclei were isolated from frozen specimens as described previously.[64] Briefly, frozen tissue samples were homogenized using a dounce homogenizer in ice-cold 30% sucrose 0.1% Triton-X 100 based homogenization buffer. 10-15 strokes of the loose dounce pestle were followed by 10-15 strokes of the tight dounce pestle on ice. Mixing using a P1000 pipette followed before filtration through a BD Falcon 40um filters. Filtration was repeated after a 10-minute spin at 1000g at 4°C. A cleanup step followed using a density gradient step as described .[65] The nuclear pellet was suspended in 1% BSA in PBS resuspension buffer containing RNAse inhibitors. A final filtration step using 20um Flowmi ™ filters followed before dilution to 700-1200 nuclei per ul in resuspension buffer. The nuclear suspensions were processed by the Chromium Controller (10x Genomics) using single Cell 3' Reagent Kit v2 or v3 (Chromium Single Cell 3' Library & Gel Bead Kit v2, catalog number: 120237; Chromium Single Cell A Chip Kit, 48 runs, catalog number: 120236; 10x Genomics).

Single nucleus RNA-seq analysis

Sequencing and analysis of raw data

Sequencing of the resultant libraries was done on Illumina NOVAseq 6000 platformV4 150bp paired end reads. We used 10X chromium v2 chemistry for samples Ctrl_1, Ctrl_2, Ctrl_3, FTD_1, FTD_2_ and FTD_3, and v3 chemistry for samples Ctrl_4, Ctrl_5, Ctrl_6, Ctrl_7, FTD_4, FTD_5, and FTD_6. Read alignment was done using the CellRanger pipeline (v5.0 - 10X genomics) to reference GRCh38.p12 (refdata-cellranger-GRCh38-1.2.0 file provided by 10x genomics). Grafts composed of human iPSC-derived neural cells were microdissected and submitted to nuclei isolation, followed by a standard single nucleus RNA-seq library preparation and sequencing.

Background removal: In each sample run (Batch), Cellranger v3 was used to map sequenced transcripts to a dual reference for human (GRCh38) and mouse (mm10).

Cellbender[66] was then used to identify and remove background from the Cellranger output ''raw_feature_bc_matrix'' file; subsequently, only cells designated with detected cell barcodes from ''filtered_feature_bc_matrix'' were used for downstream single nucleus RNA-seq data analysis using the Seurat v4.0.3 package for R.

Processing and merging

For each batch, only genes expressed in at least 10 nuclei were kept. Batches were merged into one data object and percentages of human and mouse mitochondrial genes and ribosomal-related genes were assessed, after which mitochondrial related genes for human and mouse were removed. This merged data object was then filtered, keeping only nuclei with less than 5% mitochondrial related genes, more than 1,000 and less than 25,000 unique mapped transcripts (Unique Molecular Identifiers – UMIs). For normalization of this merged data object, the Seurat function ''SCTransform'' was used to identify 3000 variable genes in all nuclei and regress out UMI counts, percent of mitochondrial genes and percent of ribosomal-related genes. 50 principal components and 20 neighbors were used to embed nuclei into a Uniform Manifold Approximation and Projection (UMAP) space for visualization and to identify cell clusters using the standard Louvain community detection algorithm implemented in Seurat. Finally, the Seurat function ''FindAllMarkers'' was used to find gene markers for cell clusters among the 3000 variable genes identified by SCTransform.

Cluster cleanup and mixed signal removal

For assessment whether a cell cluster consisted of predominantly human nuclei or mouse nuclei, gene markers for clusters were screened for human genes (GRCh38-GENE), mouse genes (mm10—Gene) or mix of human and mouse cells (GRCh38-GENE and mm10—Gene). The first round of assessment separated human clusters and mouse clusters, enabling subsetting of data objects into distinct human or mouse groups.

Subsequent re-processing of human-only data object and mouse-only data object with re-normalization, re-clustering and screening of gene markers for clusters displayed emergence of additional mixed cell clusters in both human and mouse data objects. To clean up these data objects, clusters of mouse nuclei were removed from the human data object and human nuclei clusters were removed from the mouse data object. The data objects then underwent another round of re-processing, normalization, clustering, and screening for gene markers. This entire procedure of screening and removal of species-mixed clusters was repeated until no mixed clusters were observed; 3 complete iterations were performed for the human data object and 4 iterations for the mouse data object.

In the human data object, three main cell types were observed: neurons, astrocytes and oligodendrocyte precursor cells (OPCs), based on known markers: neurons (SYT1), astrocytes (SLC1A3), OPCs (PDGFRA). The human nuclei were then split into three separate data objects corresponding to these three classes, and each of these were then re-processed, re-normalized, re-clustered, and assessed for gene markers and removal of additional cross-species clusters (whose signal was too subtle to be observed in the previous all-nuclei iterations); 2 iterations were performed for each data object to obtain final human cell-type-specific data objects. The same process was carried out for the mouse nuclei within each major cell class; 2 to 3 iterations were performed for each mouse major cell type.

For the mouse data, additional analysis was performed to identify doublet/mixed cell type clusters (as opposed to species-mixed clusters); this was done by examining gene markers representing doublet/mix cell clusters contained typical markers for two or more

major mouse cell types (e.g., astrocyte/neuron, neuron/oligodendrocyte, microglia/neuron, astrocyte/oligodendrocyte, microglia/oligodendrocyte, OPC/neuron), using the following marker genes: Astrocyte (Slc1a3), Neuron (Syt1, Slc17a7, Gad1), Oligodendrocyte (Plp1, Mog), Microglia (Dock8), OPC (Pdgfra). Clusters with mixed cell class marker genes were then removed in mouse cell type-specific data objects.

Re-merging

After these rounds of reprocessing and mixed signal removal, the resulting species- and cell type-specific data objects were re-merged in the following order: 1) human cell type-specific data objects, 2) mouse cell type-specific data objects, and 3) aggregated human and mouse data objects. This then created our final top level cell type data object with human and mouse nuclei.

Count normalization

Raw counts were normalized in Seurat using the SCT() function with default settings and controlling for percent mitochondrial and ribosomal gene expression.

Differential gene expression analysis

Differential gene expression analysis was performed in Seurat using FindAllMarkers function with default parameters.

KEGG pathway enrichment analysis

KEGG pathway enrichment analysis was done utilizing active subnetworks using pathfinder R package[54] by calling run_pathfindR() function on the differentially expressed genes. We performed the analysis on all significantly differentially expressed genes.

Pseudotime trajectory analysis

We used Monocle 3 for pseudotime cell ordering and trajectory projection onto UMAP cell embeddings obtained from single cell analysis using Seurat work flow.[55] In brief, the Seurat data object was converted to a cell_data_set object, the format accepted as input by Monocle 3 work flow. Within the Monocle 3 work flow, the cell_data_set object with Seurat UMAP cell embeddings was aligned to number of UMIs (nCount_RNA), preprocessed with PCA for UMAP dimensionality reduction and graph was learned to fully connect cells across the cell_data_set object. To order cells in pseudotime, we supervised the method and selected the Seurat cell subcluster with predominant proportion of control cells as starting point to model the trajectory projected from an unaltered/normal state towards cells with an altered/disease state in the cell_data_set object. By setting the starting point we allow for oversight of gene expression contribution across pseudotime and fluctuation along the trajectory across cells in the cell_data_set object.

QUANTIFICATION AND STATISTICAL ANALYSIS

All statistical comparisons on IHC and ISH were performed, unless otherwise indicated, in GraphPad prism. At least three samples/brains/animals per condition were used as indicated for each figure. Unpaired two-tailed t-test was used for most comparisons as indicated in the figure legends. A Multiple t-test was used in Figures 3P,3Q, 7G, S2X–S2Z′, S3S, and S5I. One-way ANOVA with Dunnett's multiple comparisons test was used in Figures 7C, S2F, and S2K–S2M. Paired t-test one-tailed was applied in Figure 7D, and unpaired t-test one-tailed was applied in Figure S4D as well as in Figures 7A, 7E–7F, 7H, 7L, 7M, 7O, S5A, S5F, and S5G to test our hypothesis of OPN function. Pairing was used for conditions from the same biological experiment. One-tailed one-sample t-test was applied in Figure 4J. Two-sample Kolmogorov-Smirnov test was used in R to compare the distributions of enrichment scores between Ctrl and FTD conditions in Figures 6G, 6L, and S6I. For quantifications of immunostainings, the investigators were blinded to conditions, and the data was unblinded after the completion of data collection.